JOINT EUROPEAN TORUS

JET–P(92)27

J.M. Adams, O.N. Jarvis, G.J. Sadler, D.B. Syme, N Watkins
and JET Team

# The JET Neutron Emission Profile Monitor

"This document contains JET information in a form not yet suitable for publication. The report has been prepared primarily for discussion and information within the JET Project and the Associations. It must not be quoted in publications or in Abstract Journals. External distribution requires approval from the Publications Officer, JET Joint Undertaking, Abingdon, Oxon, OX14 3EA, UK".

"Enquiries about Copyright and reproduction should be addressed to the Publications Officer, EFDA, Culham Science Centre, Abingdon, Oxon, OX14 3DB, UK."

The contents of this preprint and all other JET EFDA Preprints and Conference Papers are available to view online free at www.iop.org/Jet. This site has full search facilities and e-mail alert options. The diagrams contained within the PDFs on this site are hyperlinked from the year 1996 onwards.

# The JET Neutron Emission Profile Monitor

J.M. Adams[1], O.N. Jarvis, G.J. Sadler, D.B. Syme[1], N Watkins[1]
and JET Team*

***JET-Joint Undertaking, Culham Science Centre, OX14 3DB, Abingdon, UK***

*[1]AEA Industrial Technology, Harwell Laboratory, Oxon, OX11 ORA*
** See Annex*

Preprint of Paper to be submitted for publication in
Nuclear Instruments and Methods

**ABSTRACT.**

This paper provides a technical description of the neutron emission profile monitor as used routinely at the Joint European Torus (JET), and includes representative examples of its operational capabilities. The primary function of this instrument is to measure the neutron emission as a function of both position and time in a poloidal section through the torus. For the first time, sawteeth and their associated reversals have been observed using a neutron diagnostic. Comparison with other JET neutron diagnostics indicates agreement, in terms of absolute neutron emission rates, to within ±15%. This was the first such instrument routinely in use on any tokamak. It provides unique data which are independent of all other diagnostic measurements.

## *1. Introduction*

The advent of large tokamaks with increased fusion neutron production, such as the Joint European Torus (JET) [1], makes it feasible to obtain spatially-resolved measurements of the fusion neutron emission from a plasma. The knowledge of the behaviour of the neutron emissivity of the plasma, which in JET is non-circular, under different operational scenarios constitutes a powerful constraint on the theoretical modelling of the plasma behaviour.

This paper describes the design and performance capability of the JET neutron emission profile monitor, which is now used routinely to measure the fusion neutron emission during JET discharges as a function of time and of position in a poloidal section through the plasma. The work presented here is primarily concerned with performing such measurements during the D-D phase of JET operation, but the experience gained will be used to modify the instrument for the later D-T phase.

No laboratory tests of the newly-constructed profile monitor were carried out before installation on the tokamak in September 1986, as it was considered of greater importance to take advantage of a short period of operation prior to an extended shutdown, beginning November 1986, to discover whether any unexpected problems would arise from the peculiar environment of JET. In the event, a number of problems were encountered which could not have been found in laboratory tests; nevertheless, useful profile data were obtained [2].

The lessons learned in 1986 led to a number of major modifications and improvements before the re-installation of the profile monitor in August 1987. Since then, further improvements have been implemented, as deemed necessary, to cater for the increased JET fusion neutron production and to reflect the changes in the JET operational programme.

An illustration of the complete instrument as installed on JET is shown in *Fig. 1.*

## 2. *Design of the Neutron Emission Profile Monitor*

### *2.1 General Outline*

Basically, the instrument comprises 2 fan-shaped multi-collimator arrays, hereafter referred to as cameras, both viewing the same poloidal section through the plasma. The spatial resolution (fwhm) of each collimator channel at the centre of the plasma is $\approx$12cm. The horizontal camera, comprising 10 collimators and containing detector channels 1 - 10, views the vertical profile, and the vertical camera, comprising 9 collimators and containing detector channels 11 - 19, views the horizontal or radial profile. Fast neutron detectors situated at the end of each collimator channel, between 5.5 and 5.8m from the centre of the plasma, record neutron and $\gamma$-ray emission data, which are stored as time traces in the JET database.

The present multi-collimator approach was constrained by the restricted access for diagnostics on JET. The geometry ensures that each individual collimator channel has approximately the same viewing efficiency and provides a good coverage of the plasma extent (*Fig. 2*).

Unavoidably, the fusion neutron emission is slightly attenuated by the structural materials (mainly Inconel 600) of the vessel access and pumping port windows. In addition, neutrons backscattered from, and $\gamma$-rays produced at, the interior vessel walls and central column contribute directly to the events recorded in each collimator channel detector.

### *2.2 Neutron and Gamma-ray shielding*

Both cameras utilise bulk high density concrete shielding assemblies [a] (a composition of barytes, colemanite and portland cement with a density of $\approx$3400 kg/m$^3$) within which is located a removable detector box housing the

a) supplied by Sir Robert McAlpines, Hayes, Middlesex, England ; and Python Cranes, Littleborough, Lancashire, England.

neutron detectors, plus a removable high density concrete rear shield to reduce background neutrons and $\gamma$-rays backscattered from the external JET structure and torus hall walls.

The horizontal camera assembly (*Fig. 3*) consists of a bulk shield ($\approx$3.1m $\times$ 1.5m $\times$ 2.1m) weighing $\approx$32 tonnes, supported with its centre line at a height of 6m above the torus hall floor by a steel tower. The vertical camera assembly (*Fig. 4*) consists of a bulk shield ($\approx$1.55m $\times$ 1.0m $\times$ 1.75m) weighing $\approx$12 tonnes, and is supported on brackets attached to the upper horizontal limbs of the magnetic structure of JET. In the case of the vertical camera assembly, both the bulk and removable shield assemblies have additional lead screens to reduce the $\gamma$-ray flux associated with the nearby water cooling pipework.

Inside both bulk shields are embedded the mild steel channel collimators, of rectangular cross-section. Those in the horizontal camera all measure 44 $\times$ 25mm, with provision for collimator inserts to reduce the aperture to 24 $\times$ 15mm, 15 $\times$ 15mm or 10 $\times$ 10mm, dependent upon the JET operational programme. Those in the vertical camera vary from 25 $\times$ 8mm (channel 11) up to 25 $\times$ 25mm (channel 19) due to the geometrical constraints of viewing the plasma in a narrow triangular opening through the vertical port structure, with provision for 15 $\times$ 15mm or 10 $\times$ 10mm collimator inserts in the wider channels. For both cameras, the detector boxes are located behind 1200mm of high density concrete.

### *2.3 Fast Neutron Detection*

Although the detection of 2.45 MeV neutrons, even in the presence of $\gamma$-rays, is fairly straightforward in principle, the JET environment poses several problems with regard to the choice of a suitable neutron detector. In particular, the fusion neutron emission rate and the effect of the high and variable magnetic fields around JET have to be considered.

In the D-D phase of JET, the total fusion neutron yield ranges up to $5 \times 10^{16}$ n/s, which implies a direct neutron flux of up to $\approx 10^7$ n/s in the central channels

of the instrument, plus associated $\gamma$-ray and backscattered neutron contributions. Consequently, the neutron detection system has to have :

- a fast response to achieve good time resolution,
- a capability to discriminate between neutrons and $\gamma$-rays,
- a reproducible neutron energy bias to provide a stable neutron detection efficiency; the setting to be chosen to reduce the backscattered neutron component to an acceptable level.

A neutron detector based on the NE213 liquid organic scintillator [b] coupled to a pulse shape discrimination (PSD) unit [c] was chosen to satisfy these requirements.

### *2.4 Magnetic fields*

Measurements of the magnetic field strengths at the proposed neutron detector locations for the horizontal and vertical cameras during several JET discharges ($B_T \approx 3.4T$ ; $I_P \approx 5MA$) prior to installation indicated that magnetic fields of up to 0.01 and 0.1T, respectively, would be experienced by the neutron detectors. Photomultiplier tubes, although usually supplied enclosed in an open $\mu$-metal cylinder, are highly susceptible to magnetic fields (including the Earth's at $\approx 5 \times 10^{-5}$ T) and, therefore, must be well shielded against the high variable magnetic fields in the vicinity of JET.

The solution to the problem of how to operate scintillation detectors in such high magnetic fields involved a series of closed cylinders, and using materials with progressively increasing magnetic permeability, whilst ensuring that no cylinder was allowed to become magnetically saturated. This resulted in the design of a triple magnetic shield comprising mild steel (3mm in the horizontal camera and 8mm in the vertical camera), 2mm radiometal [d] and 1.2mm $\mu$-metal [d], as shown

b) supplied by NE Technology Ltd., Sighthill, Edinburgh, Scotland.

c) supplied by Link Analytical Ltd., High Wycombe, Bucks., England.

d) supplied by Telcon Metals Ltd., Crawley, Sussex, England.

in *Fig. 5*. The mild steel cylinders in the vertical camera were also electrically insulated from the detector box housing to eliminate magnetic break-through.

### *2.5 Temperature*

The ambient temperature in the JET torus hall is $\approx 25°C$, rising to $> 30°C$ when JET is operational. The gain of photomultiplier-based detectors varies with the environmental temperature. The use of a triple magnetic shield to overcome the high variable magnetic fields meant that the photomultipliers were located in a fully-enclosed confined space. Due to heat dissipation in the detector dynode chains, it was found necessary to apply water cooling to the outside of the individual mild steel cylinders to maintain the detectors at a constant temperature (in the range 12 to 18°C) and to employ various techniques for monitoring the temperature and individual detector operation.

In the event of a failure in the cooling water supply, resulting in an increase in the detector temperature, the system has been designed to trip the high voltage detector supply at a pre-definable temperature (usually $\approx 20°C$).

## *3. Experimental System*

The complete electronic arrangement for the neutron emission profile monitor is shown schematically in *Fig. 6*. The cable distance from the detector box housings to the main instrument conditioning electronics is 60m, and from the conditioning electronics to the CAMAC data acquisition electronics is a further 50m.

### *3.1 Neutron detector / PSD combination*

Each fast neutron detector comprises an NE213 liquid organic scintillator (50mm diameter × 10mm deep bubble-free BA-1 cell), with a small built-in $^{22}Na$ source ($\approx 200$ nanocurie), coupled to a 5cm diameter 10-stage low-gain low-noise Thorn-EMI 9815 linear focussed photomultiplier. The output signals are DC

coupled (*via* 60m 75Ω superscreened coaxial cable [e]) to Link Analytical Model 5020 Pulse Shape Discriminator units to distinguish between neutron and $\gamma$-ray events.

Smaller NE213 cells (25mm diameter × 10mm deep) have recently been introduced for high neutron yield discharges in order to reduce the detection volume of the cells not in the direct channel line-of-sight when using the smaller collimator inserts, so as to minimise the extraneous background component.

### *3.2 Fast Neutron Detector*

It is important to match the photomultiplier gain to the input requirements of the PSD unit to achieve optimum neutron / $\gamma$-ray discrimination performance. The photomultiplier dynode chain voltage divider was specifically designed for use with this PSD unit, based on several years of experience with such units in fast neutron time-of-flight applications [3].

### *3.3 Pulse Shape Discrimination (PSD) Unit*

The Link Analytical Model 5020 PSD unit (an improved Model 5010) is essentially that described by Adams and White [3], but with the outputs and logic modified for the present application to enable a higher throughput.

The PSD unit has 4 independently variable discriminator levels, *viz.* THRESHOLD, PILE-UP, LOWER and UPPER. The THRESHOLD discriminator determines the input stage constant fraction discrimination level and sets the minimum input signal processed by the PSD unit. The PILE-UP discriminator determines the signal level for the rejection of events due to pile-up in the scintillator at high count rates. The LOWER discriminator level is set to the desired operational neutron energy bias and the UPPER discriminator level is set at the desired upper neutron energy bias. Together, the LOWER and UPPER discriminator levels define the energy windows corresponding to the

e) MM20/75 supplied by BICC, Helsby, Warrington, England; and Cabeltel, Fumay, France

NEUTRON and GAMMA digital pulse outputs. Neutron events above the UPPER discriminator level are output as UPPER events. (This latter output was provided as a special modification, by Link Analytical, to the standard Model 5020 PSD unit).

In addition, the PSD units used in this application have a remote control feature, also implemented by Link Analytical, which enables both the selection of any of the 19 PSDs and the type of ANALOGUE output (ALL, NEUTRON, GAMMA or UPPER) in order to provide measurements of the energy spectra for diagnostic performance monitoring and physics purposes.

PSD digital outputs corresponding to NEUTRON and GAMMA events in the neutron energy range 2 to 3.5MeV (equivalent to a $\gamma$-ray energy range of $\approx$0.7 to 1.44MeV) and UPPER neutron events above $\approx$ 3.5MeV, plus LIVETIME CORRECTION, are fed, *via* TTL-ECL converters, to 4 separate latching scalers (Lecroy Model 4433) with (normally) 10ms time resolution for subsequent storage in the JET database. In addition, there is provision for recording specific time-sliced (0.5s) ANALOGUE output data from one channel PSD per discharge, to be digitised and stored in the form of a sequence of spectra.

The built-in $^{22}Na$ source is used to set the appropriate neutron energy biases and to facilitate monitoring of the detector.

The calibration for each detector is obtained in terms of the equivalent neutron energy by recording the pulse height spectrum from the built-in $^{22}Na$ source and establishing the channel numbers corresponding to the peak and half-heights of the 2 Compton edges. In terms of electron energy, this corresponds to 0.303 and 0.350 MeV for the 0.511 MeV $\gamma$-rays and 0.994 and 1.077 MeV for the 1.274 MeV $\gamma$-rays from $^{22}Na$. The equivalence between $\gamma$-ray and neutron energy was derived from monoenergetic neutron response function measurements in the energy range 1.5 to 3.3 MeV performed on the 5MV Van de Graaff [4] at Harwell Laboratory by bombarding a thin ($\approx$5keV thick) *TiT* target with protons in the energy range 2.4 to 4.2 MeV. The relation determined from these measurements can be expressed in the quadratic form given by

$$L_p(E_p) = -0.131 + 0.25E_p + 0.03915E_p^2 \quad (1.5 \leq E_p \leq 3.3\ MeV)$$

where $L_p$ is the equivalent electron energy (MeVee), and $E_p$ is the maximum recoil proton energy (MeV). These measurements were necessary since the relation of Cecil *et al.* [5] was found to be inappropriate for the NE213 scintillators used in the present application. The results are in excellent agreement with the more recent work of Dekempeneer [6], but not with that of Verbinski [7].

The spectrum zero offset channel is determined directly by recording a pulse height spectrum with the PSD unit switched to ALL, which corresponds to all events above the THRESHOLD discriminator level plus the built-in stabilisation pulse. A typical $^{22}Na$ pulse height spectrum is shown in *Fig. 7*, which indicates the equivalence between corresponding neutron and $\gamma$-ray events in terms of their equivalent electron light output response in relative units.

### *3.4 Magnetic Field Monitoring*

Within each detector box, there are 2 triple-axis magnetic field probes (each comprising 3 sets of 100 turn coils at right angles) to measure the magnetic field outside the neutron detector assemblies. The magnetic fields are sampled using a 10ms time resolution for each discharge, and stored as time traces in the JET database.

### *3.5 Temperature Monitoring*

Within each detector box there are 3 RTD temperature sensors [f], 2 strapped to different detectors, and 1 monitoring the internal detector box temperature. These sensors are sampled at $\approx$15s intervals irrespective of whether a discharge is in progress and the values at the end of each discharge are stored in the JET database.

f) supplied by H.A.Wainwright & Co. Ltd., Guildford, Surrey, England.

## 4. Corrections to the Experimental Data

The basic data recorded by the neutron emission profile monitor comprises the time-traces of the individual channel line-integrated emissions corresponding to neutron and $\gamma$-ray events. The following have to be considered:

- livetime correction,
- neutron detection efficiency,
- geometry, which includes solid angle,
- neutron attenuation and collimator scattering,
- neutron backscatter, and
- cross-talk between adjacent channels.

### 4.1 Livetime Correction

The PSD LIVETIME CORRECTION output differs from the normal BUSY output in that it compensates for the rejection of events occurring within the pulse integration time. This output is used to gate a free-running high precision oscillator (2MHz); departures from 2MHz determine the correction for dead-time.

### 4.2 Neutron Detection Efficiency

The absolute neutron detection efficiency was determined using conventional associated particle techniques on the Harwell 500kV Van de Graaff, utilising the $D(d,n)^3He$ and $D(d,p)T$ reactions. For a neutron energy bias of 2 MeV, the absolute neutron detection efficiency for 2.45 MeV neutrons was measured to be $2.4 \times 10^{-2}$ per neutron/cm$^2$.

As well as requiring a good knowledge of the absolute detection efficiency of each individual neutron detector, it is also important in this application to know the relative efficiency responses between the 19 detector / PSD combinations. Measurements with a strong $^{252}Cf$ source, first with a single detector combined with each PSD, and then using each detector combined to the same PSD unit,

showed all relative detector / PSD combination efficiency responses to be the same to within ±2-3%.

### *4.3 Geometry*

The experimental neutron emission rate, $(n/s)$, is converted to line-integrated neutron emissivity, $(n/s/m^2)$, using the factor $(ab)^2/4\pi l^2$ where $a$ and $b$ are the collimator widths, and $l$ the collimator length.

### *4.4 Neutron Attenuation and Collimator Scattering*

Corrections are required for: (i) the attenuation of the neutrons as they pass through the vacuum vessel windows and the material surrounding the neutron detector, and (ii) the scattering of the neutrons in the collimator itself. A detailed MCNP [8] model of each profile monitor channel has been used to calculate the combined correction for each channel. For the horizontal camera, the correction is ≈9% and for the vertical camera ≈17.5%. The differences are due to the different thicknesses of neutron attenuating materials between the neutron producing plasma and the fast neutron detectors.

### *4.5 Neutron Backscatter*

A different correction for neutron backscattering is needed for each individual collimator channel since they look directly at the inner wall of the JET vacuum vessel from which scattered neutrons emanate. These correction factors were calculated using the FURNACE [9] code. It was found that, for a neutron energy bias of 2 MeV, the backscattered neutron contribution in the central channels amounts to ≈3% of the total incident neutron flux on the detector, rising to >75% in the outer channels. The backscatter contribution increases significantly with decreasing neutron energy bias.

### *4.6 Cross-talk*

Cross-talk can arise from neutrons entering one channel being scattered in the neutron detector region and, subsequently, being detected in the neutron detector in an adjacent channel. Measurements using a strong *Am-Be* source, positioned at the entrance to one collimator, showed the cross-talk to be $< 0.5\%$. As a result no corrections to the data are needed.

### *4.7 Summary*

In principle, the application of the above corrections should be straightforward, as certainly appears to be the case for Ohmic and low power Ion Cyclotron Resonance Heating (ICRH) discharges, but has still to be fully quantified for the high fusion neutron yield discharges. The problem here is to understand the various $\gamma$-ray breakthrough and pile-up effects which are strongly dependent upon both the total detector count rate and the $n/\gamma$ ratio at a given bias. ($\gamma$-ray breakthrough is the erroneous recognition of $\gamma$-ray events as neutron events by the PSD unit, and increases at both lower biases and higher rates).

## *5. Data Assessment and Analysis*

Because of the vast amount of data ($> 0.5$ Megabytes) recorded for each JET discharge, a dedicated computer code with enhanced graphics capabilities has been written to allow a detailed assessment and preliminary analysis of the data to be carried out in a variety of formats, including:

- individual neutron and $\gamma$-ray emission time traces,
- horizontal and vertical camera neutron and $\gamma$-ray emission profiles,
- horizontal and vertical camera neutron and $\gamma$-ray emission contour plots (profile v. time),
- comparison with global measurements (fission chambers) [10-12],
- centroid of neutron emission (global geometry correction factors),
- specific neutron and $\gamma$-ray energy spectra (one channel per discharge),
- time dependence of the magnetic fields within the detector boxes.

## 6. *Operational Capabilities*

As this instrument was the first neutron emission profile monitor to be operated routinely on any tokamak, it is useful to present some representative examples of the data to illustrate its operational capabilities and the benefits of having good spatial and time dependent information for the neutron emission during a discharge.

More detailed analyses of some of the data so far obtained using this instrument have already been described in the literature [13-16].

### *6.1 Time Traces and Profiles*

*Fig. 8* shows the time traces for the neutron signals from a typical 5MA Ohmic D-D plasma discharge over a period of 17s for all of the 19 channels. The first two rows refer, in order, to the horizontal camera channels and the remainder to the vertical camera channels. *Fig. 9* shows the corresponding horizontal camera neutron emission profiles (*i.e.* vertical profiles) in 1s intervals. As would be expected, the neutron emission is greatest in the central channels indicating that the main fusion neutron production occurs in the central regions of the plasma. By contrast, as would be expected, the $\gamma$-ray emission (not shown) is essentially channel independent, since it primarily arises from neutrons escaping from the vacuum vessel and interacting with the surroundings, although some are from neutron interactions with the interior vessel walls within the view of the collimators.

However, during some JET discharges a significant $\gamma$-ray component has been observed that is attributable to $\gamma$-ray emission from the plasma itself. *Fig. 10* compares neutron and $\gamma$-ray emissions during periods of Ion Cyclotron Resonance Heating (ICRH) and Neutral Beam Injection (NBI) within the same discharge; it is clear that ICRH can be accompanied by a large increase in $\gamma$-ray emission without a corresponding increase in the neutron emission. In such cases, the $\gamma$-rays emanating from the plasma are due to ICRH accelerated (up to several

MeV) charged particles which induce nuclear reactions with the plasma contaminants, mainly *Be, C* and *O* [13,14].

### *6.2 Sawtooth Phenomena*

Examination of the individual channel time traces for many deuterium discharges reveals the sawtooth phenomenon in the central channels, accompanied by sawtooth reversals in some of the outer channels, as shown in *Fig. 11.* In many instances the peak-to-valley ratio of individual sawteeth is 3 to 1. Since this is a line integral representation, the axial neutron emissivity must exhibit even more dramatic changes during sawteeth oscillations in the plasma. *Fig. 12* shows the neutron emission profile before and after a sawtooth crash using 2.5ms time resolution.

In the main, the $\gamma$-ray time profiles do not exhibit this phenomenon during deuterium discharges, since the $\gamma$-rays originate primarily as a result of neutron capture in the vessel walls and surroundings. However, $\gamma$-ray sawteeth and their associated reversals have been observed [13,14] during ICRH due to interaction of fast (MeV) RF driven particles with *Be, C,* and *O* impurities in the plasma (*Fig. 13*).

### *6.3 Major Plasma Disruptions*

During a major plasma disruption, the instantaineous detector count rate can be extremely high due to run-away electrons interacting with first wall components, and may result in excessive $\gamma$-ray breakthrough in the neutron channels. This aspect of the data has yet to be fully examined. Nevertheless, the data do indicate clear differences in the disruption duration and often indicate where the run-away electrons (created during the disruption) strike the vessel wall.

### *6.4 Runaway Electron Dominated Plasmas*

*Fig. 14* illustrates the interaction of run-away electrons with one of the protection tiles on the inner vessel wall early in a JET discharge. Similar time traces are observed in the more central channels, but less so in the outer channels.

Another such phenomenon, shown in *Fig. 15*, is unique to the wall area around the bottom diagnostic port viewed by channel 14 from which both high neutron and $\gamma$-ray emission are observed; there are no signals in the other channels. Incidentally, this provides further evidence in support of the observation (see 4.6 above) that the cross-talk between detectors is minimal.

## *7. Comparison with other JET Neutron Diagnostic Data*

The neutron emission profile data have been compared with data from the JET time-resolved neutron monitor [10-12] which consists of 3 pairs of fission chambers mounted on the vertical linbs of the transformer yoke in the mid-plane of the machine. The spatial neutron emission information is used to correct the fission chamber data for the geometric effects of the plasma position in the computation of the absolute JET neutron emission as a function of time during the discharge. *Figs. 16 & 17* illustrate the variation in the total neutron emission ratio between the neutron emission profile and time-resolved neutron monitors by considering separately the neutron emission summations for each camera. *Fig. 16* relates to an NBI discharge (2.5MW of 80keV $D^o$) where the ratios are essentially constant, whereas *Fig. 17* relates to a combined NBI and ICRH discharge (18MW NBI ; 12MW ICRH) where there is a ratio inbalance due to excessively high count rate effects in the neutron emission (due to $\gamma$-ray breakthrough) and the production of neutrons in the range up to 10 MeV as a result of nuclear reactions with plasma contaminants. It should be noted that a strong component of non D-D fusion neutrons with energies appreciably above 3 MeV will also be detected, but with a lower efficiency than the 2.45 MeV neutrons. However, neutrons below $\approx$2 MeV will not be detected at all. (For

D-D operation the contribution due to the 1% D-T fusion neutrons can be ignored).

## *8. Discussion*

The initial 1986 tests of this instrument, primarily aimed at assessing overall performance, were extremely fruitful. The main concern was that about half the NE213 liquid organic scintillators had developed bubbles due to operating the detectors for long periods at temperatures $>35°C$. This led to a complete re-build of the vertical camera detector box housing, the installation of adequate water cooling for all detectors, complete re-wiring of the detector dynode chains, the replacement of all NE213 scintillator cells, and improved inter-channel neutron shielding. Since the re-installation in 1987, the instrument has recorded neutron emission data during most discharges for all JET operational scenarios involving significant fusion neutron production. The reliability of the electronics has been high with only occasional PSD malfunctions, and bubbles in the NE213 cells.

The D-D plasma data clearly exhibit the sawtooth oscillation phenomenon previously observed by many other plasma diagnostics, and, for the first time with neutron diagnostics, the associated sawteeth reversals. Clearly, this is an area in which exploitation of neutron emission profile monitor can and will be usefully pursued.

Comparison between the neutron emission profile and time-resolved neutron monitors in terms of their total neutron emission ratio shows consistency within the errors for Ohmic and low power NBI and ICRH discharges. However, this ratio deviates by up to 20% from a constant value with increasing fusion neutron production, the effect being particularly pronounced when the ICRH system is used because of $\gamma$-ray breakthrough (leading to an apparent increase in the number of neutron events) and the detection of neutrons from nuclear reactions of fast RF-driven minority ions with plasma contaminants.

At present there is one major problem that has yet to be fully resolved for the highest yield deuterium discharges when the instrument is operating close to its maximum count-rate capability in both cameras ($\approx$500kHz) even after reducing the size of the collimator apertures. An increasingly high $\gamma$-ray breakthrough is observed, this being particularly pronounced during periods of intense ICRH when the $\gamma$-ray emission from the plasma itself is high. In addition, the high density concrete shielding is evidently inadequate as a high $\gamma$-ray background is observed which is unaffected by the reduction in collimation. A number of measures have been introduced to reduce this $\gamma$-ray component, including surrounding the complete detector box housing with $\approx$5cm of lead, using lead filters inside the collimators, and reducing the potential for $\gamma$-ray streaming at various points on the bulk shielding. None of these measures has resulted in a satisfactory reduction. However, the employment of smaller scintillators has reduced the unwanted background events in proportion to the volume of scintillant outside of the direct channel line-of-sight.

The PSD technique has been extensively used for many applications, but there is minimal information on its performance at rates above $\approx$200kHz., at which the $\gamma$-ray breakthrough was measured to be 1-2% using a strong $^{60}Co$ source [3]. This increases rapidly with count-rate. The various associated pile-up contributions can affect the $n/\gamma$ ratio quite dramatically, resulting in an increase in the number of events erroneously recorded as neutrons. Pile-up has the following consequences :

- $n$-$n$ : detected as a neutron with a larger proton recoil energy,
- $n$-$\gamma$ : detected as a neutron with a larger proton recoil energy,
- $\gamma$-$n$ : detected as a neutron with a larger proton recoil energy,
- $\gamma$-$\gamma$ : a fraction will be detected as neutrons dependent upon the PSD integration times and the relative neutron and $\gamma$-ray event pulse decay times.

In terms of absolute neutron emission, comparison with the absolute determination of the neutron yield from the global neutron monitoring diagnostics indicates agreement (under favourable conditions) to within $\pm$15%. The observed departures of up to $\pm$30% are a result of $\gamma$-ray breakthrough effects

and the detection of neutrons from nuclear reactions with plasma contaminants. In addition, within the dynamic energy range of the neutron emission profile monitor, the detection efficiency is a function of the neutron energy. On the other hand, the global neutron monitors (*i.e.* fission chambers) are equally sensitive to neutrons of all energies (below 20 MeV), and are fairly insensitive to $\gamma$-rays.

The original design of the instrument was also aimed at the tomographic reconstruction of the neutron emission profile data, which, although not considered here, has been addressed by Marcus *et al* [16]. *Fig. 18* shows a representative tomographic reconstruction of the neutron emission profile monitor data before and after a sawtooth crash.

## *9. Conclusions*

The neutron and $\gamma$-ray emissions have been recorded for most JET operational scenarios that result in significant fusion neutron production. A number of features have become clearly evident and have convincingly demonstrated that measurements of neutron emission as a function of position and time in the same poloidal section through the plasma are important.

The operational experience gained from the instrument in its present form provides a firm foundation for more detailed exploitation during the next phase of JET operations. However, the high count rate problems experienced require to be resolved before the commencement of the JET D-T phase. This will necessitate replacement of the NE213 cells with other detectors more suitable for the high yields of D-T fusion neutrons, together with improvements to the neutron and $\gamma$-ray shielding configurations.

## *Acknowledgements*

The design, construction and commissioning of this instrument by Harwell Laboratory, has been funded under a number of JET contracts. The authors are indebted to a number of people at JET, Harwell, and elsewhere, who have been involved to varying degrees at the various stages: to M.T.Swinhoe (Harwell) who was largely responsible for the initial outline design; P.Dixon (Harwell) for the design and manufacture of the bulk shield assemblies and their associated supports; G.B.Huxtable (Harwell) for the design and R.Oliver-Hall (Harwell) for the manufacture of the TTL-ECL converters and PSD analogue multiplexer; P. van Belle (JET) for the design and manufacture of the PSD channel selector and PSD mode selector modules, and for invaluable discussions pertinent to interfacing with the JET database; S.Duroux (JET) for the design and manufacture of the magnetic field probe control unit; M.Hone (JET) for the procurement *etc.* of the temperature and magnetic field measuring probes; and G.White (Link Analytical) for numerous discussions, design changes and continuing interest relating to the optimisation of the PSD units pertinent to this instrument.

Finally, the various members of the Neutron Diagnostics Group and Support Staff at JET for the installation of the diagnostic in the Torus Hall, the provision of the requisite cabling, and the associated CAMAC data-acquisition system.

## *References*


1. E.N.Shaw, Europe's Experiment in Fusion, The JET Joint Undertaking, North-Holland (1990) ; Fusion Technology, **11**, (1987), 7-281.

2. J.M.Adams, O.N.Jarvis, J.Kallne, G.Sadler, D.B.Syme, M.T.Swinhoe, N.Watkins, P. van Belle and K.Verschuur, 14th EPS Conference on Controlled Fusion and Plasma Physics, Madrid, 22-26 June 1987.

3. J.M.Adams and G.White, Nucl. Instr. Meth., **156**, (1978), 479.

4. P.M.Read and J.M.Stevens, Nucl. Instr. Meth., **A249**, (1986), 141.

5. R.A.Cecil, B.D.Anderson and R.Madey, Nucl. Instr. Meth., **161**, (1979), 439.

6. E.Dekempeneer and H.Liskien, Nucl. Instr. Meth. in Physics Research, **A256**, (1987), 489.

7. V.V.Verbinski, W.R.Burrus, T.A.Love, W.Zobel and N.W.Hill, Nucl. Instr. Meth., **65**, (1968), 8.

8. A General Purpose Monte Carlo Code for Neutron and Photon Transport, LA-7336-M, Los Alamos National Laboratory, (1981).

9. K.A.Verschuur, ECN-86-097, ( Petten, June 1986 ) ; and private communication.

10. M.T.Swinhoe and O.N.Jarvis, Nucl. Instr. Meth. in Phys. Res., **221**, (1984), 460.

11. M.T.Swinhoe and O.N.Jarvis, Rev. Sci. Instrum., **56**, (1985), 1093.

12. O.N.Jarvis, G.Gorini, M.Hone, J.Kallne, V.Merlo, G.Sadler and P. van Belle, Europhys. Conf. Abstracts, Vol 9F, Part 1, p223, (1985).

13. G.Sadler, O.N.Jarvis, P. van Belle and J.M.Adams, 15th EPS Conference on Controlled Fusion and Plasma Physics, Dubrovnik, 16-20 May 1988, Vol 1, p131.

14. G.Sadler, S.Conroy, O.N.Jarvis, P. van Belle, J.M.Adams and M.Hone, Fusion Technology, **18**, (1990), 556.

15. J.M.Adams, A.Cheetham, S.Conroy, G.Gorini, N.Gottardi, T.Iguchi, O.N.Jarvis, G.Sadler, P.Smeulders, N.Watkins and P. van Belle, 16th EPS Conference on Controlled Fusion and Plasma Physics, Venice, 13-17 March 1989, Vol 13B, Part 1, p63.

16. F.B.Marcus, J.M.Adams, A.Cheetham, S.Conroy, W.G.F.Core, O.N.Jarvis, M.J.Loughlin, M.Olsson, G.Sadler, P.Smeulders, P.van Belle and N.Watkins, 17th EPS Conference on Controlled Fusion and Plasma Heating, Amsterdam, 25-29 June 1990, Vol 14B, Part 1, 331.

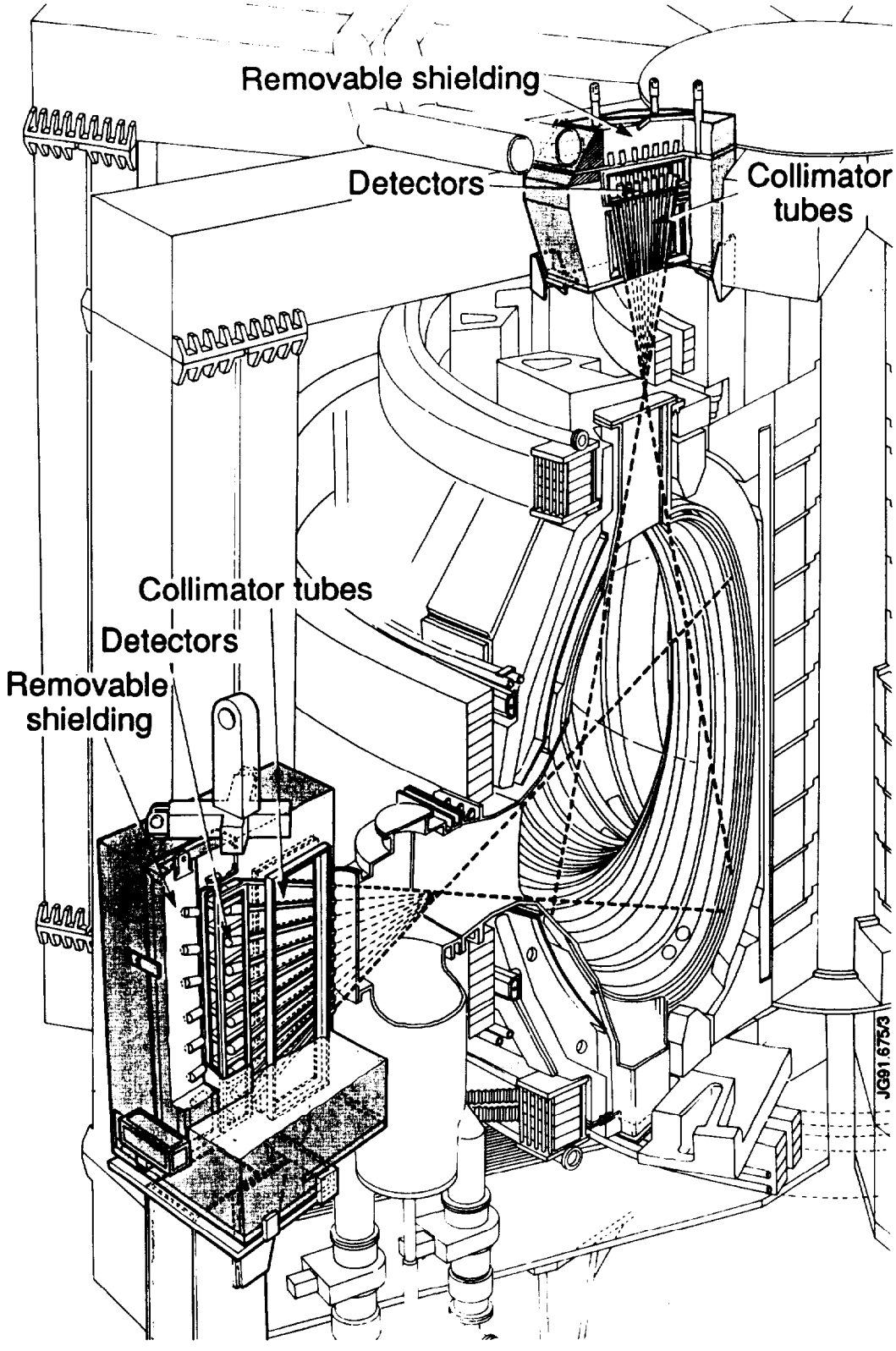


1. Artist's Impression of the JET Neutron Emission Profile Monitor. The location of the 2 bulk shield assemblies are shown relative to the main structure of JET.

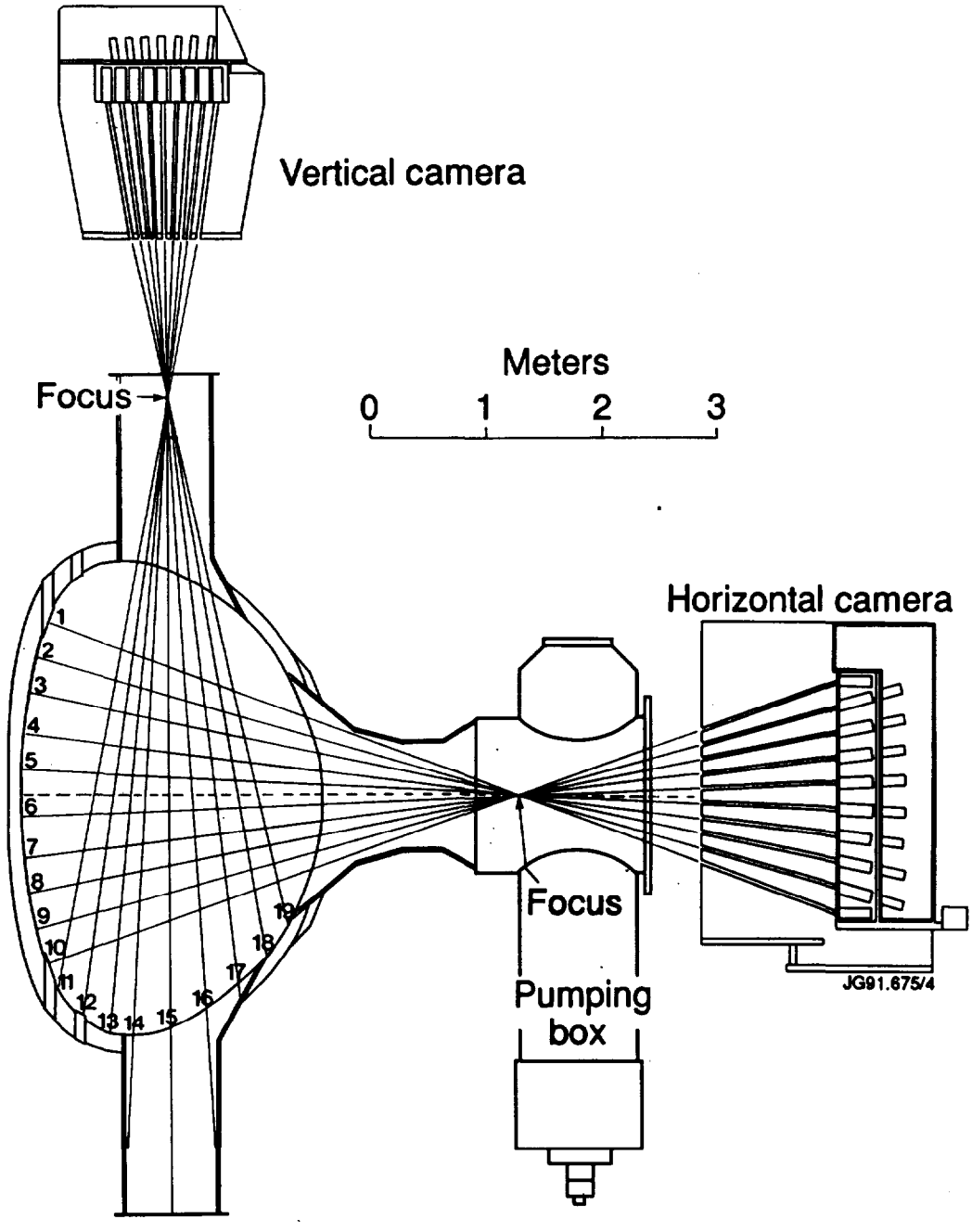


2. Schematic of the JET Neutron Emission Profile Monitor Collimation Geometry. The direct line-of-sight chords illustrate the overall viewing extent within the JET vacuum vessel.

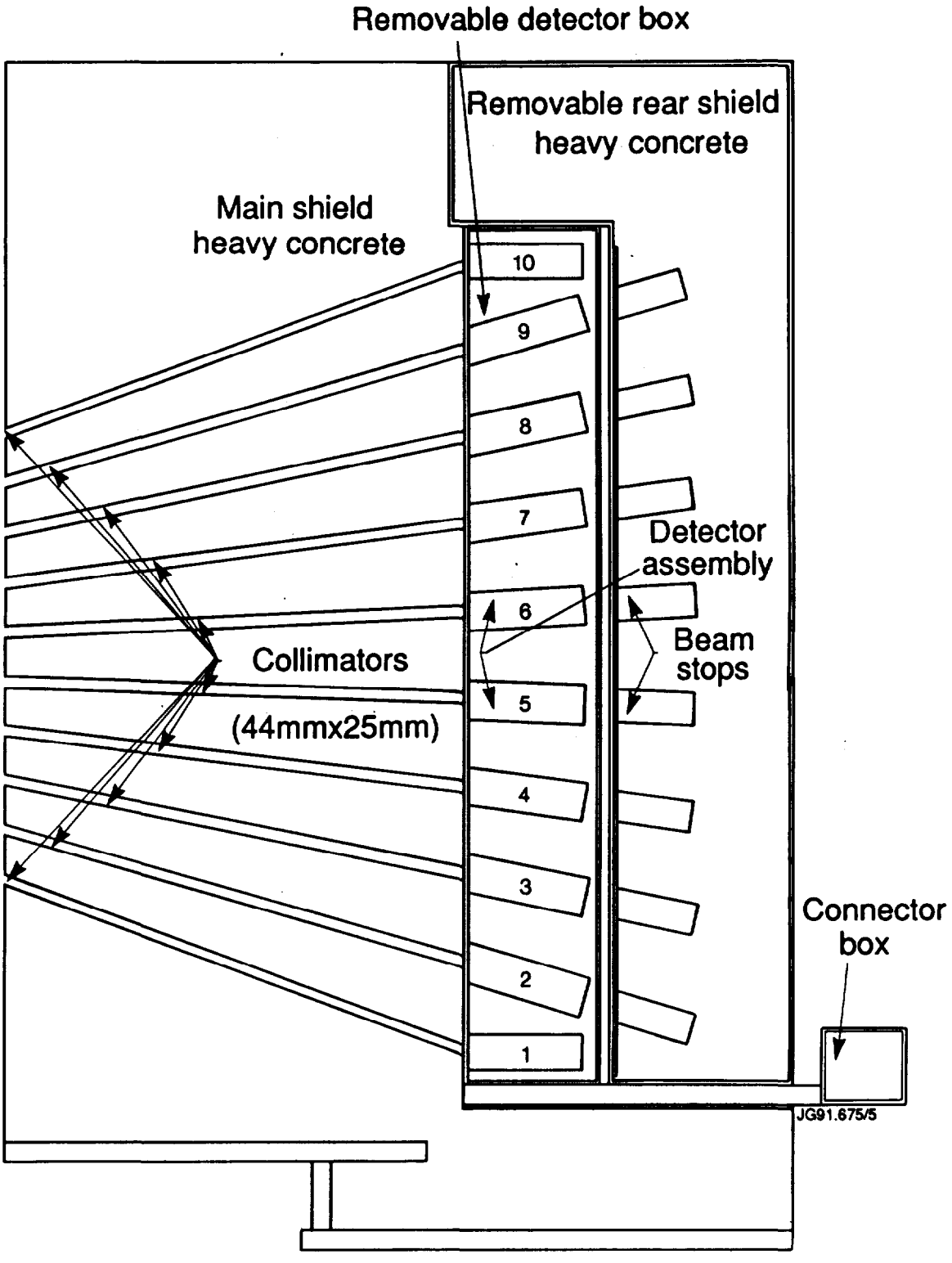


3. Horizontal Camera Shield Assembly ( ≈32 tonnes ). The location of the removable detector box and rear shield are shown relative to the main bulk shield in which are embedded the 10 collimator channels. The removable rear shield contains the neutron beam dumps for 8 of the 10 channels.

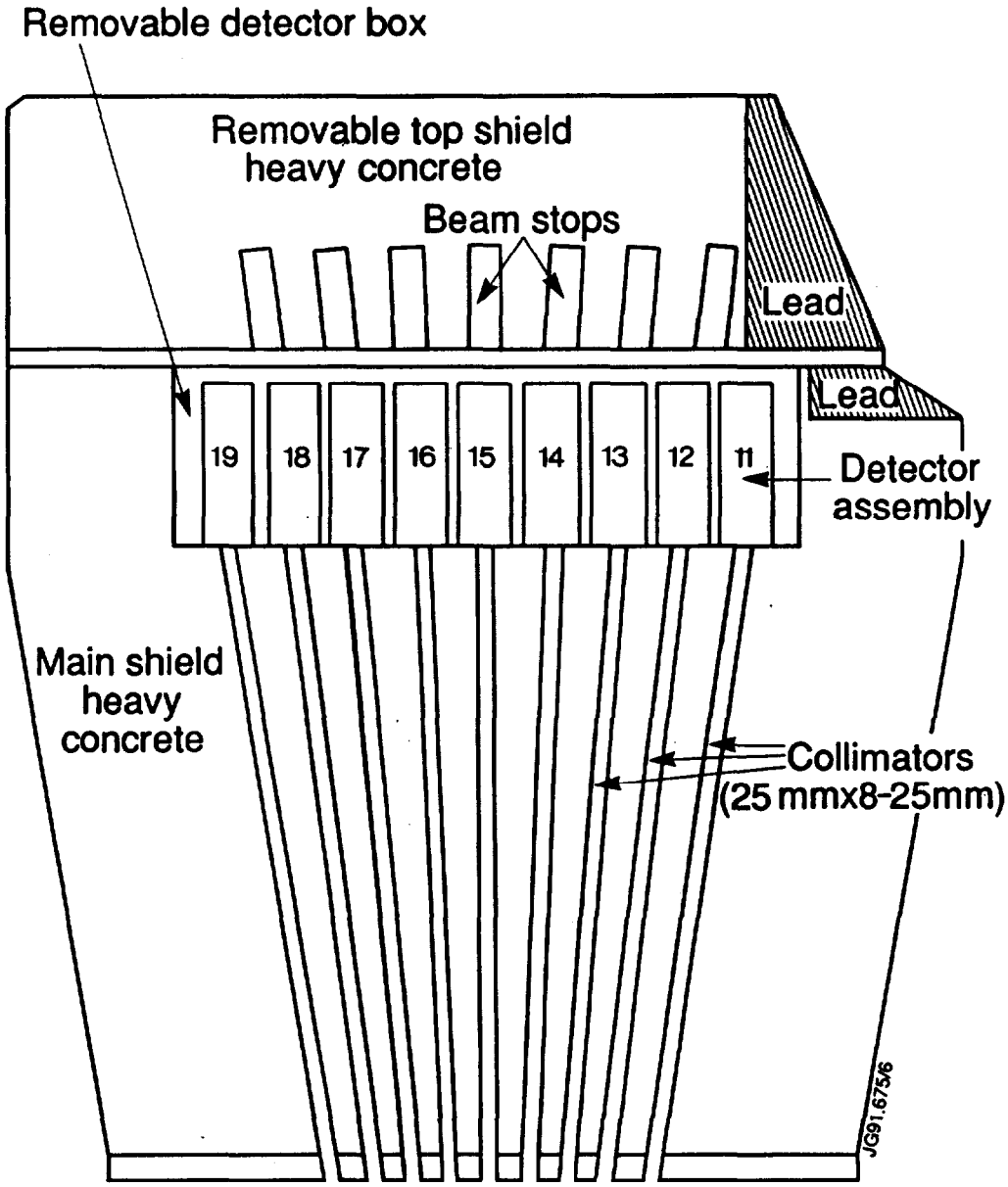


4. Vertical Camera Shield Assembly ( $\approx$12 tonnes ). The location of the removable detector box and top shield are shown relative to the main bulk shield in which are embedded the 9 collimator channels. The removable top shield contains the neutron beam dumps for 7 of the 9 channels. Additional lead shielding is included to shield against $\gamma$-rays emitted from the adjacent watercooling pipe.

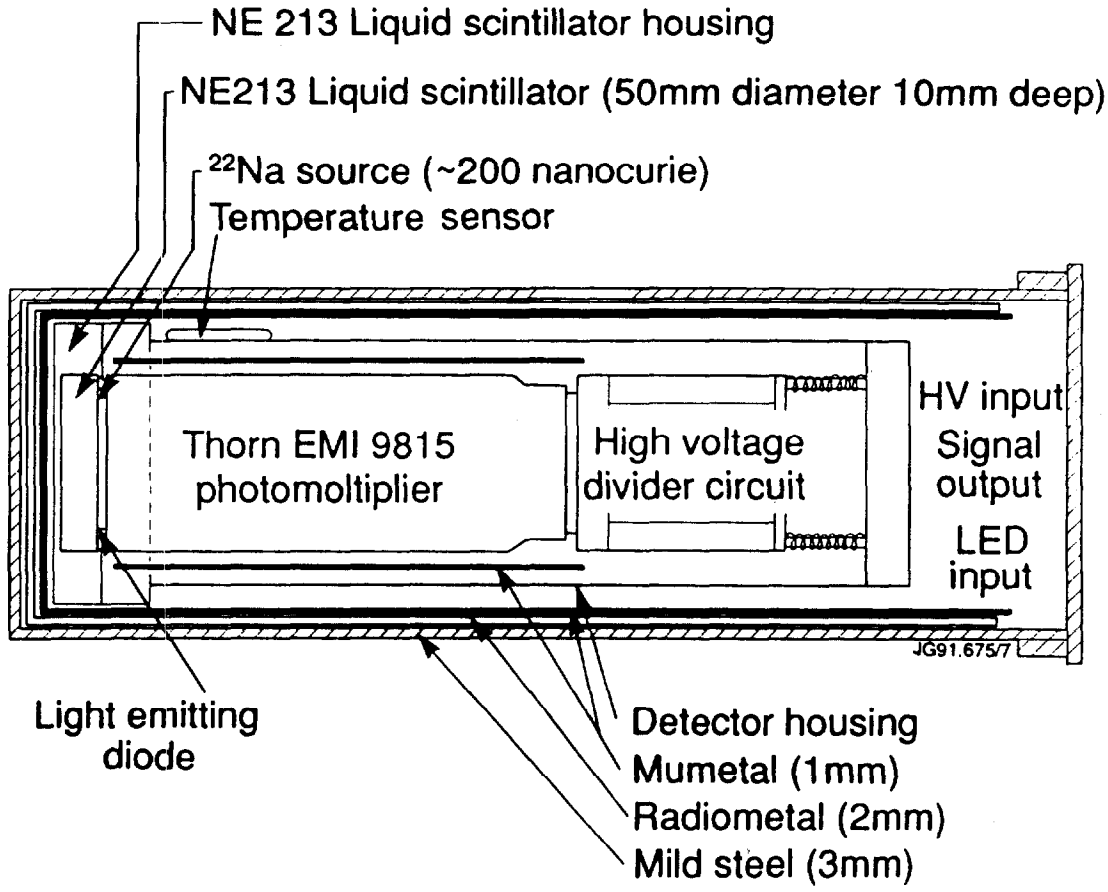


5. Fast Neutron Detector and Triple Magnetic Shield Assembly. This illustrates the magnetic shielding around the neutron detector necessary for operation in the highly fluctuating magnetic fields in the vicinity of JET.

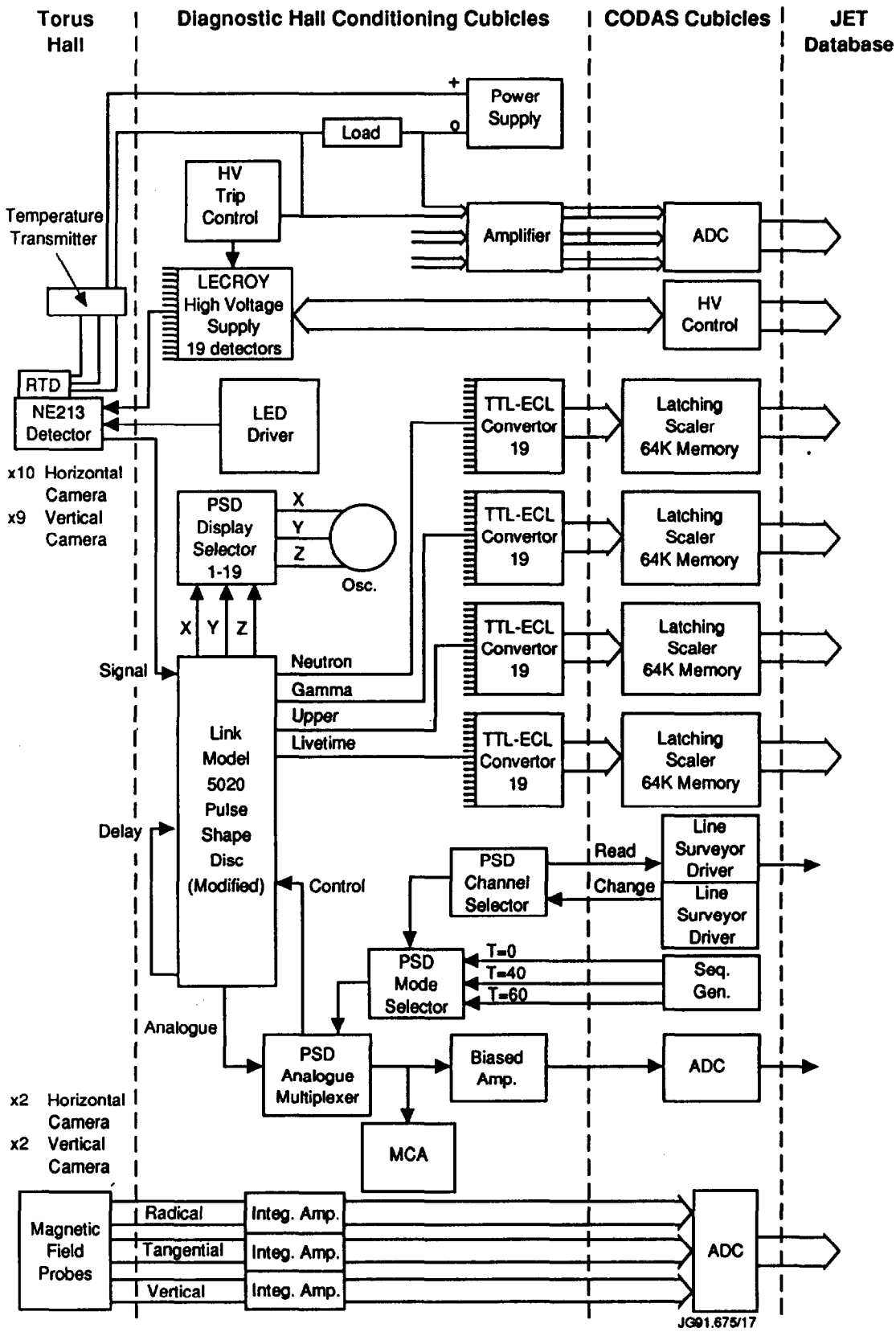


6. Electronic Schematic of JET Neutron Emission Profile Monitor. This shows the complete electronic configuration for one neutron detector channel, and its relation to the communal data acquisition modules for storage in the JET database.

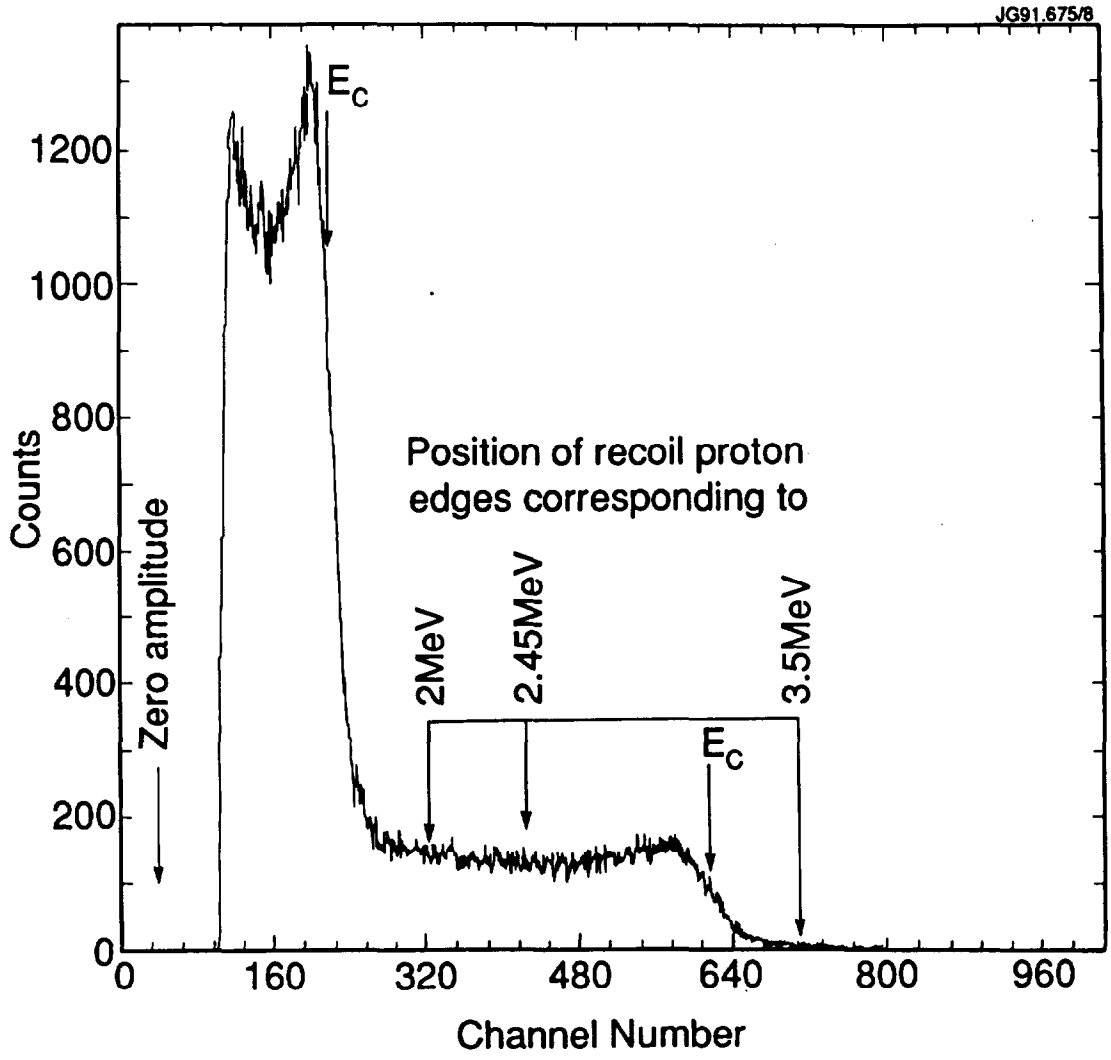


7. $^{22}$Na Pulse Height Spectrum showing Neutron Energy Equivalence. This illustrates the relationship between neutrons and $\gamma$-rays in terms of their equivalent electron energies. The neutron energy bias monitoring technique adopted requires that the UPPER discrimination level be set above the Compton edge of the 1274keV $\gamma$-rays from $^{22}$Na.

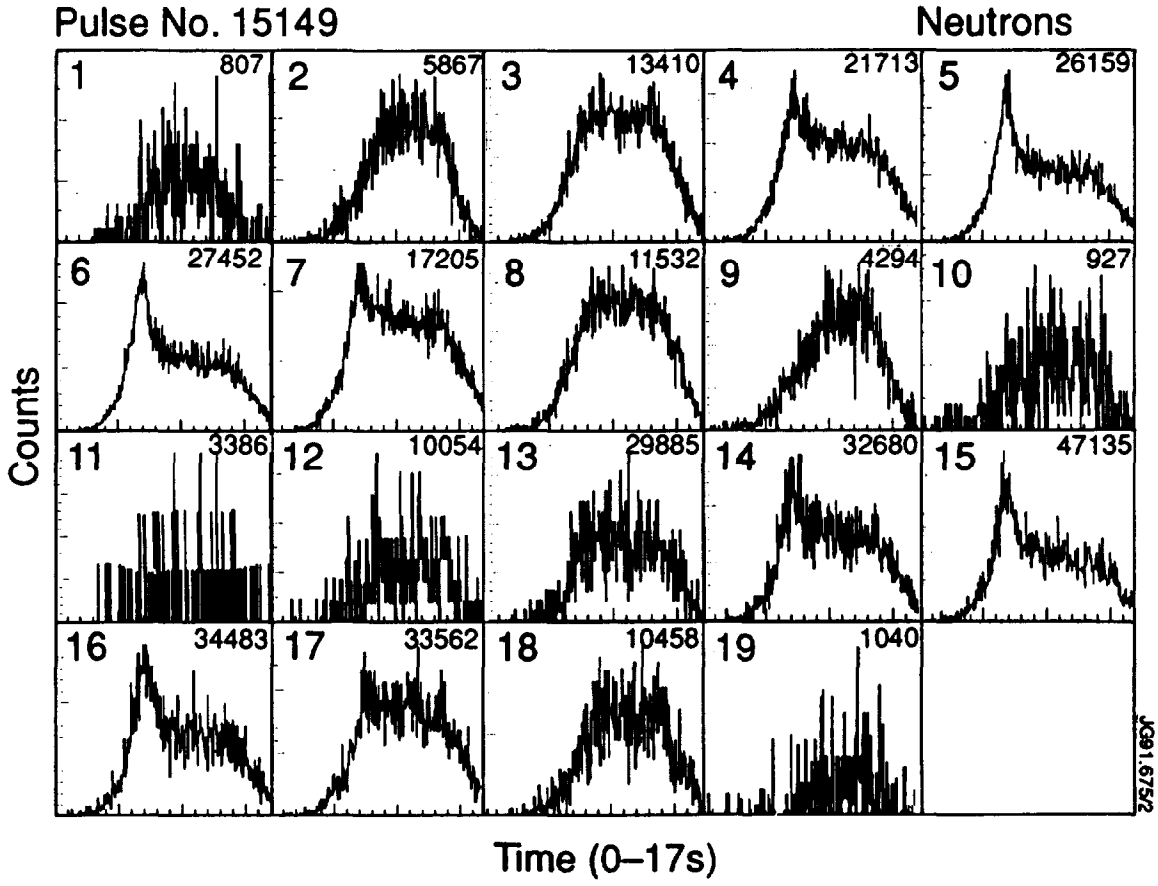


8. Time Dependence of the Neutron Emission in the 19 Individual Channels for a Deuterium Fuelled 5MA Discharge. The traces are corrected for neutron detection efficiency etc. The channel numbers are indicated in the top left hand corners. The total neutron emission observed in the individual channels during the 17s period are indicated in the top right hand corners.

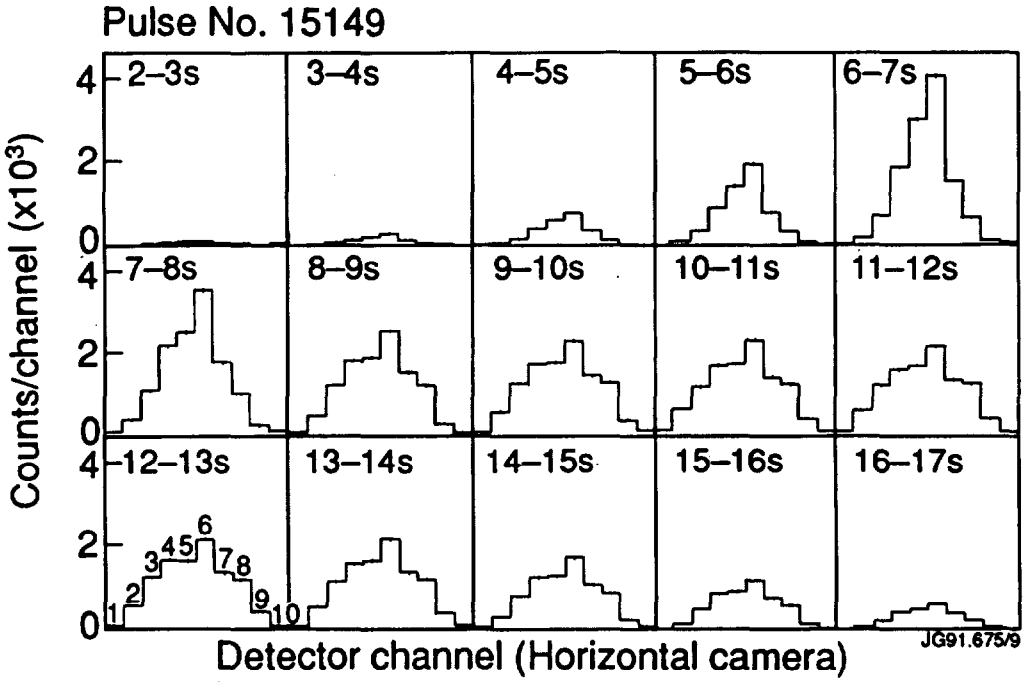


9. Neutron Emission Profiles as seen by the Horizontal Camera in 1s Intervals for the Same Discharge as shown in *Fig. 8*. Time intervals are marked at the top of each profile and the channel number correspondance is indicated in the bottom left hand profile.

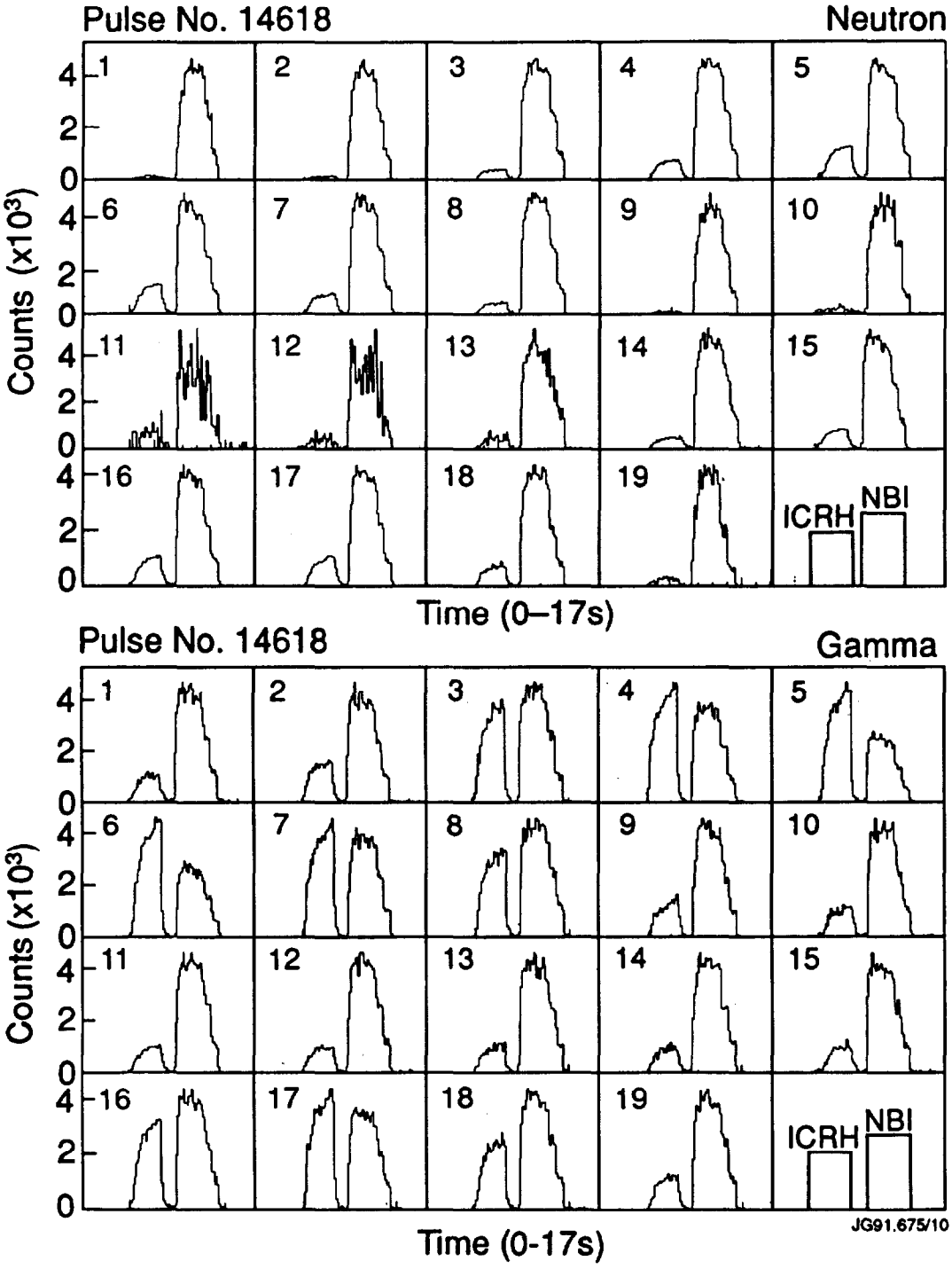


10. Comparison of Neutron and $\gamma$-ray Emission Time Traces during Periods of ICRH (9.5MW $^3$He) and NBI (8MW of 80keV D$^o$). Channel numbers are given in the top left hand corners. The final trace shows the heating waveform. It is clear that the $\gamma$-ray emission in the central channels is strongest during the ICRH period whereas the neutron emission in all channels is strongest during the NBI heating period.

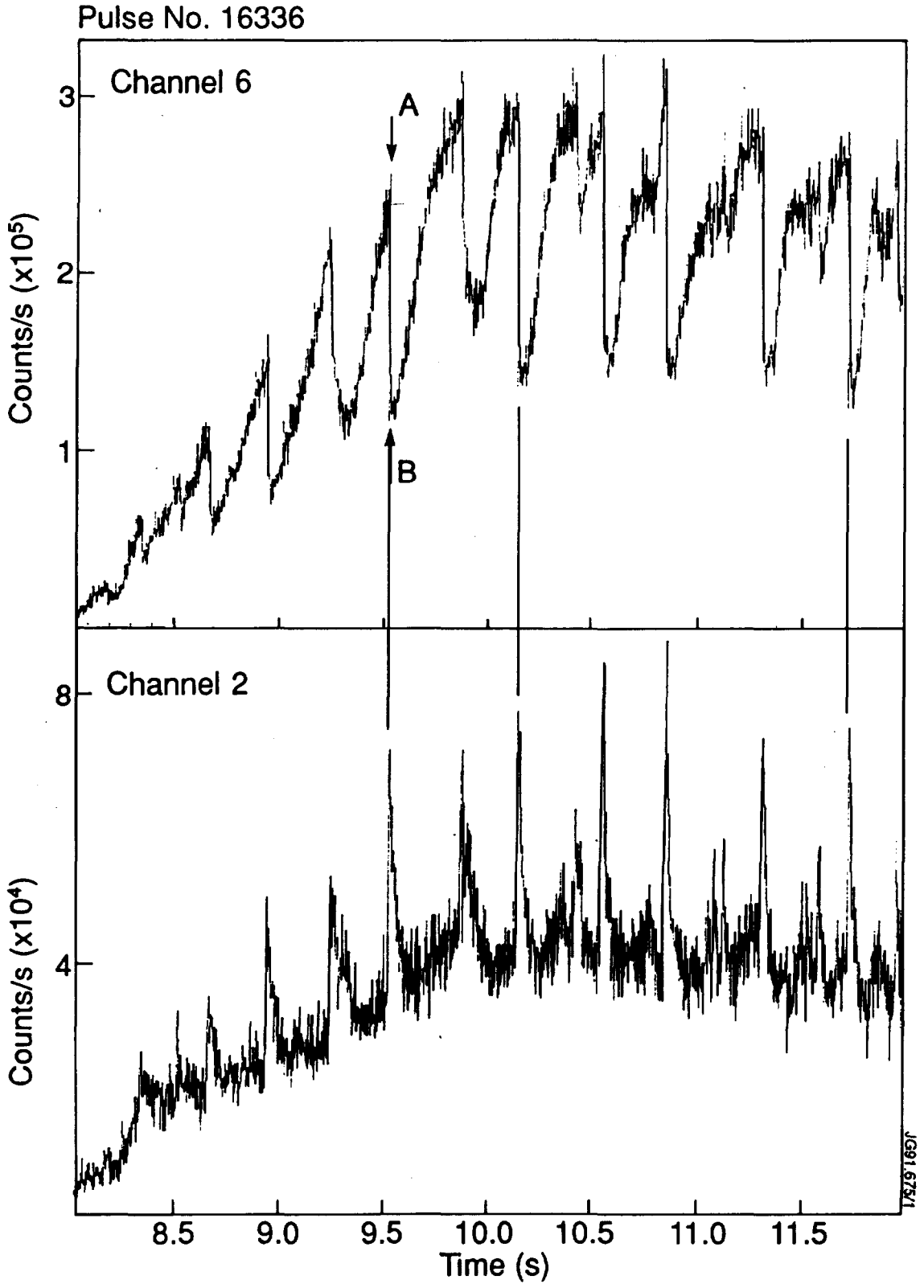


11. Neutron Sawteeth as observed in a Central Channel (Channel 6) and Associated Reversals from an Outer Channel (Channel 2) for a 5MA Deuterium Fuelled Discharge with 9MW of ICRH and 6MW of NBI Heating. The data were acquired in 2.5ms intervals.

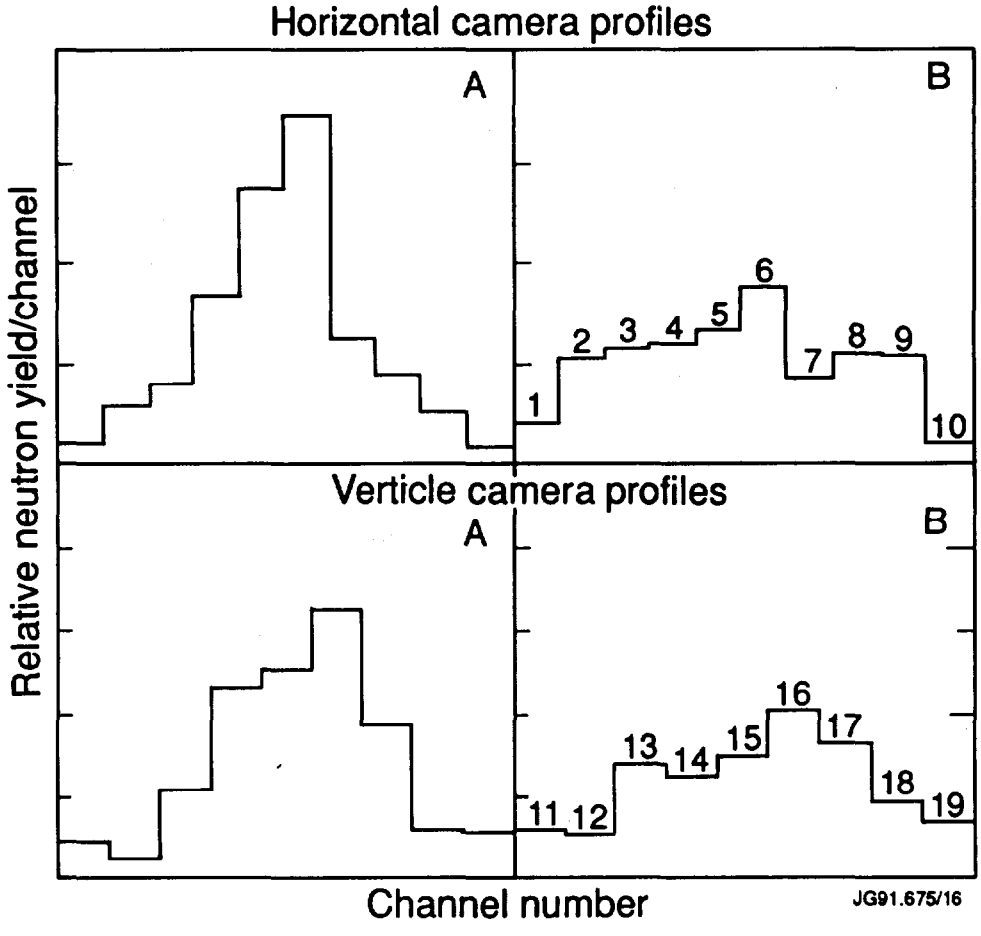


12. Neutron Emission Profiles during a 2.5ms Time Interval Before and After the Sawtooth Marked in *Fig. 11*.

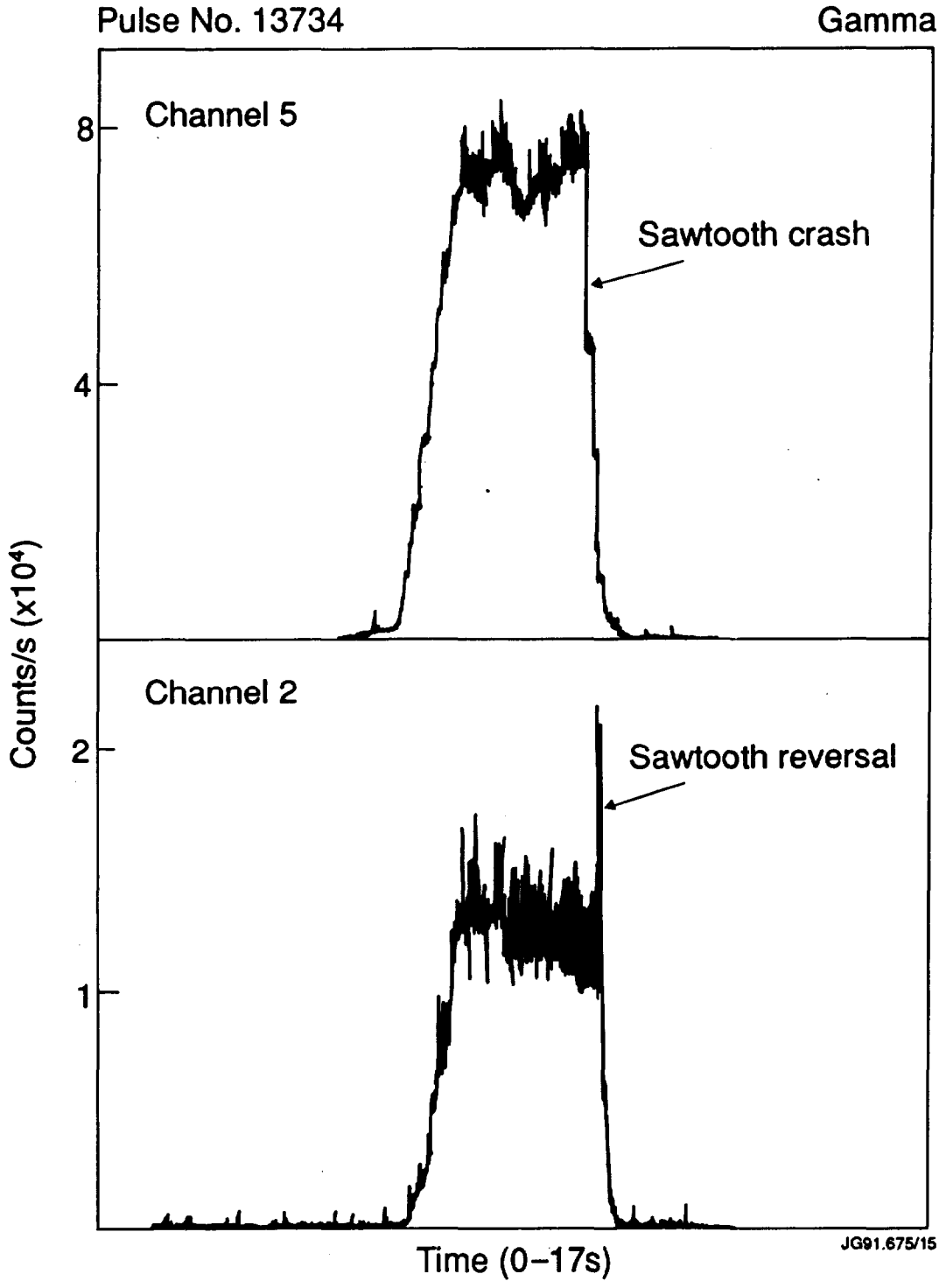


13. A Monster Sawtooth Crash as observed by the $\gamma$-ray Channels 5 and 2. A clear reversal is seen in Channel 2. The observed $\gamma$-rays are due to interactions of energetic RF driven (11MW) $^3$He ions (E > 1MeV) interacting with C impurity ions in the plasma. At the sawtooth crash these fast particles are expelled from the centre of the plasma causing the abrupt increase in $\gamma$-ray detection in the outer channels.

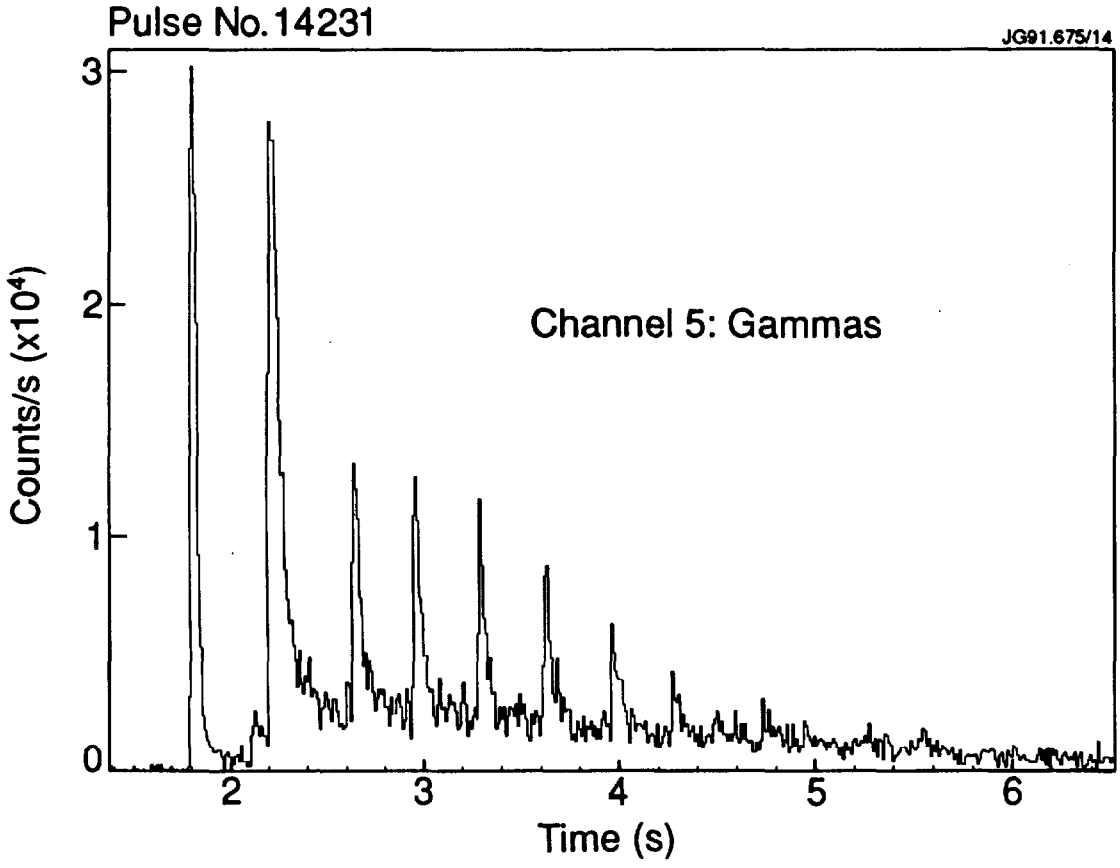


14. Example of a Run-away Electron Dominated Discharge. The periodic interaction of the fast (up to 60 MeV) electrons with the first wall components leads to the generation of bursts of hard X-ray Bremsstrahlung, which is detected in the $\gamma$-ray channels of the cameras.

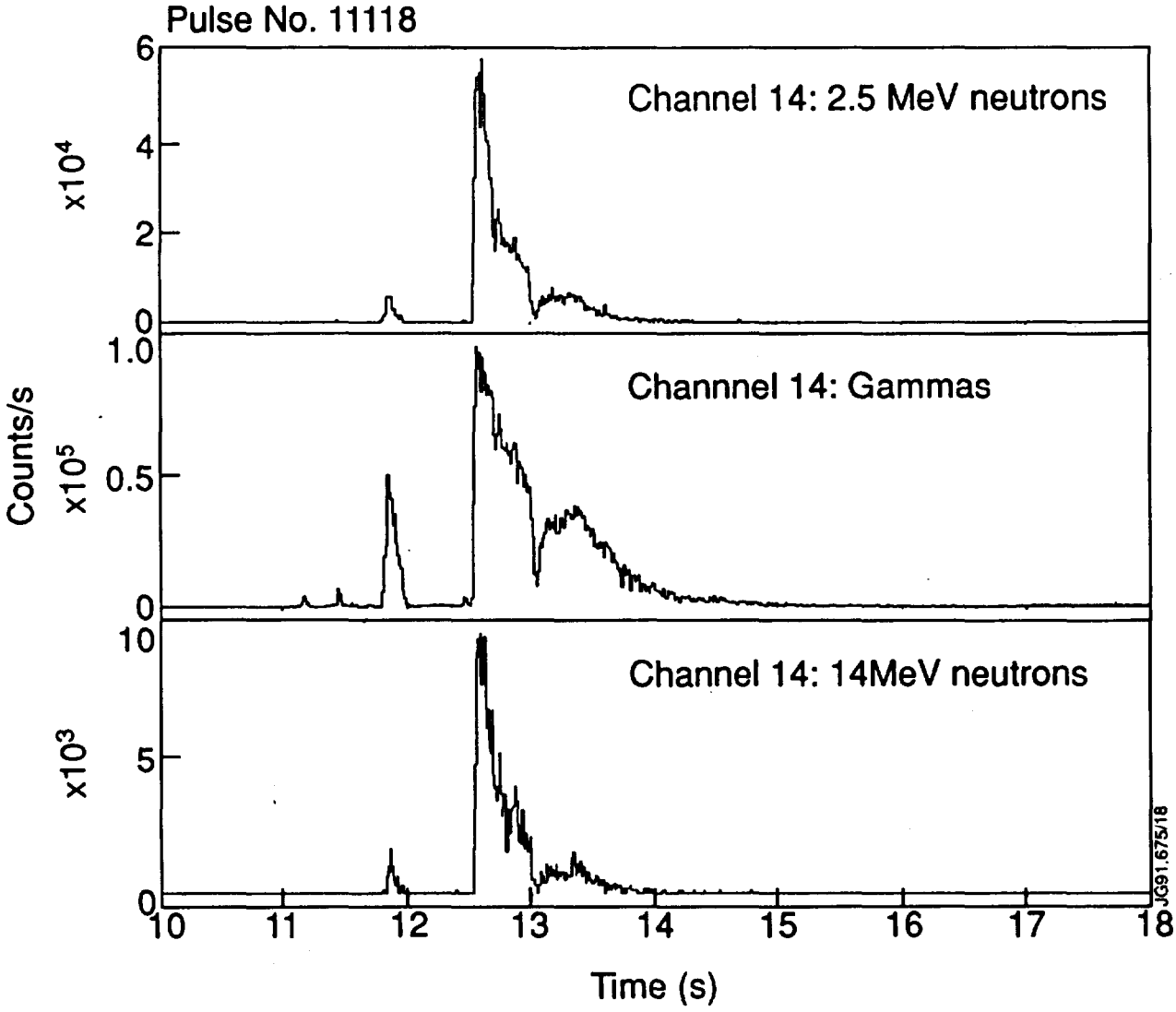


15. Example of Run-away Electrons Observed only in Channel 14. Run-away electrons interact locally with first wall material opposite the line-of-sight of Channel 14 to form bursts of hard X-rays (identified as $\gamma$-rays by the PSD unit) and photoneutrons.

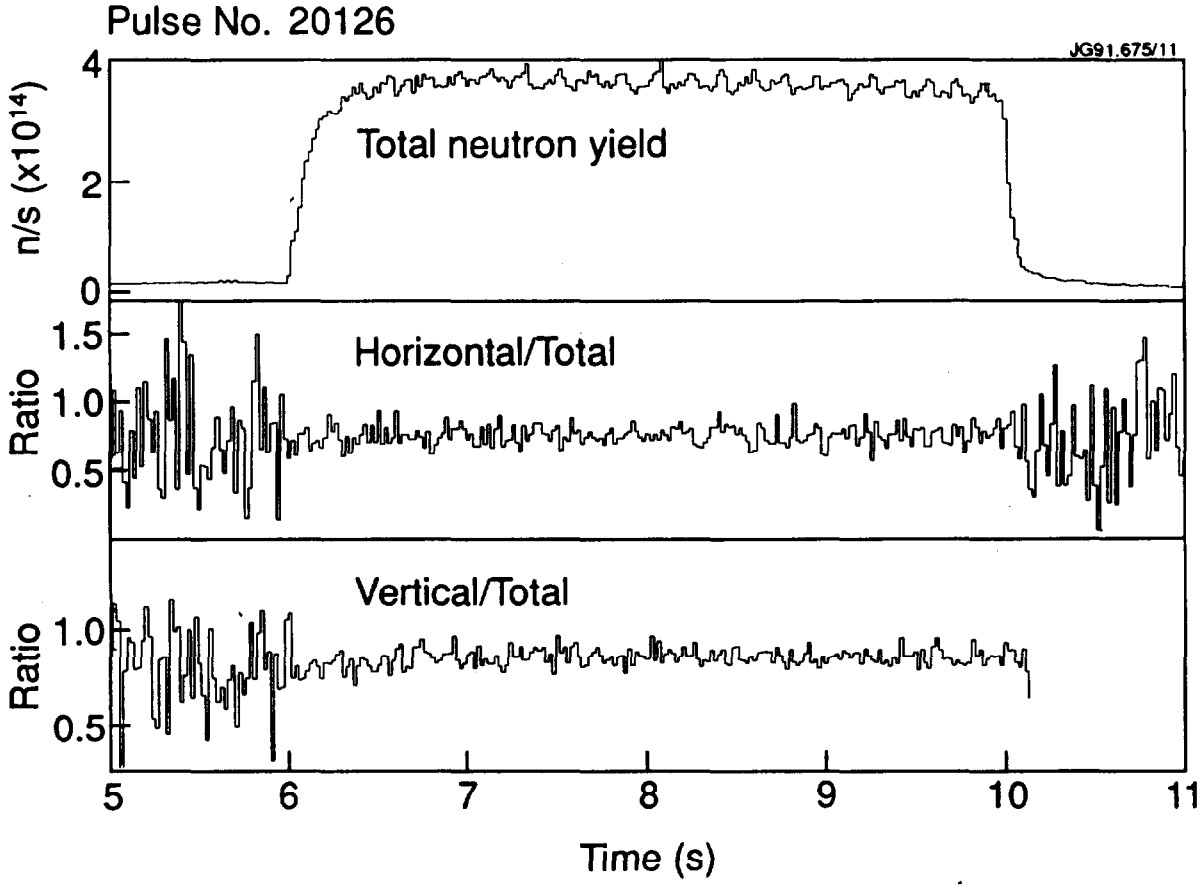


16. Ratios of Measured Neutron Emission for a 2.5MW NBI Discharge. The upper time trace shows the global neutron yield as determined by the time-resolved fission chambers. The middle and lowermost time traces show, respectively, the ratio between the individual camera summations and the global neutron yields. In this case the ratio is constant during the whole of the discharge period associated with significant fusion neutron production.

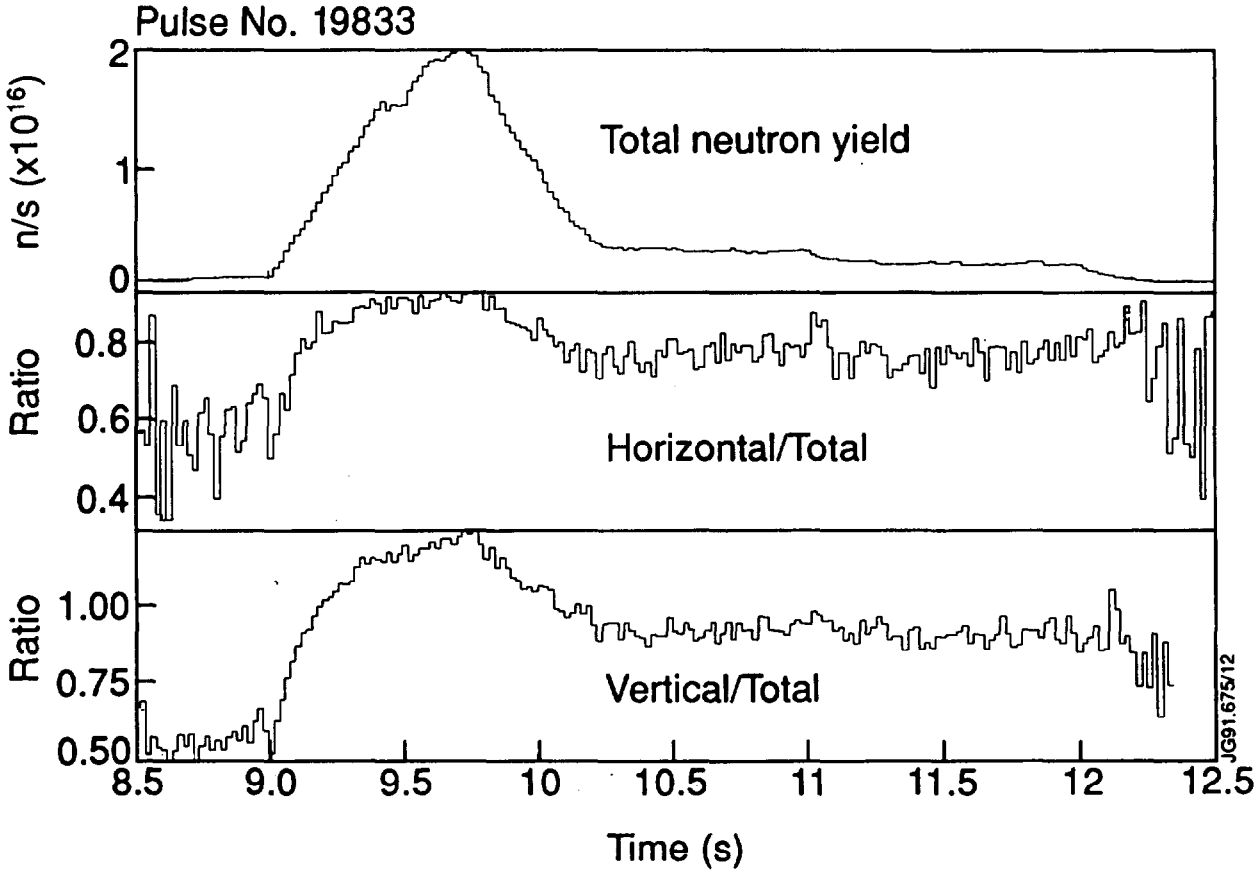


17. Ratios of Measured Neutron Emission for a combined 18MW NBI and 12MW ICRH Discharge. In this case the ratio deviates significantly from a constant during the period of maximum fusion neutron production due to $\gamma$-ray breakthrough effects and the detection of neutrons resulting from nuclear reactions with plasma contaminants. Note the low values during the period before 9s while only ICRH was applied to preheat the plasma.

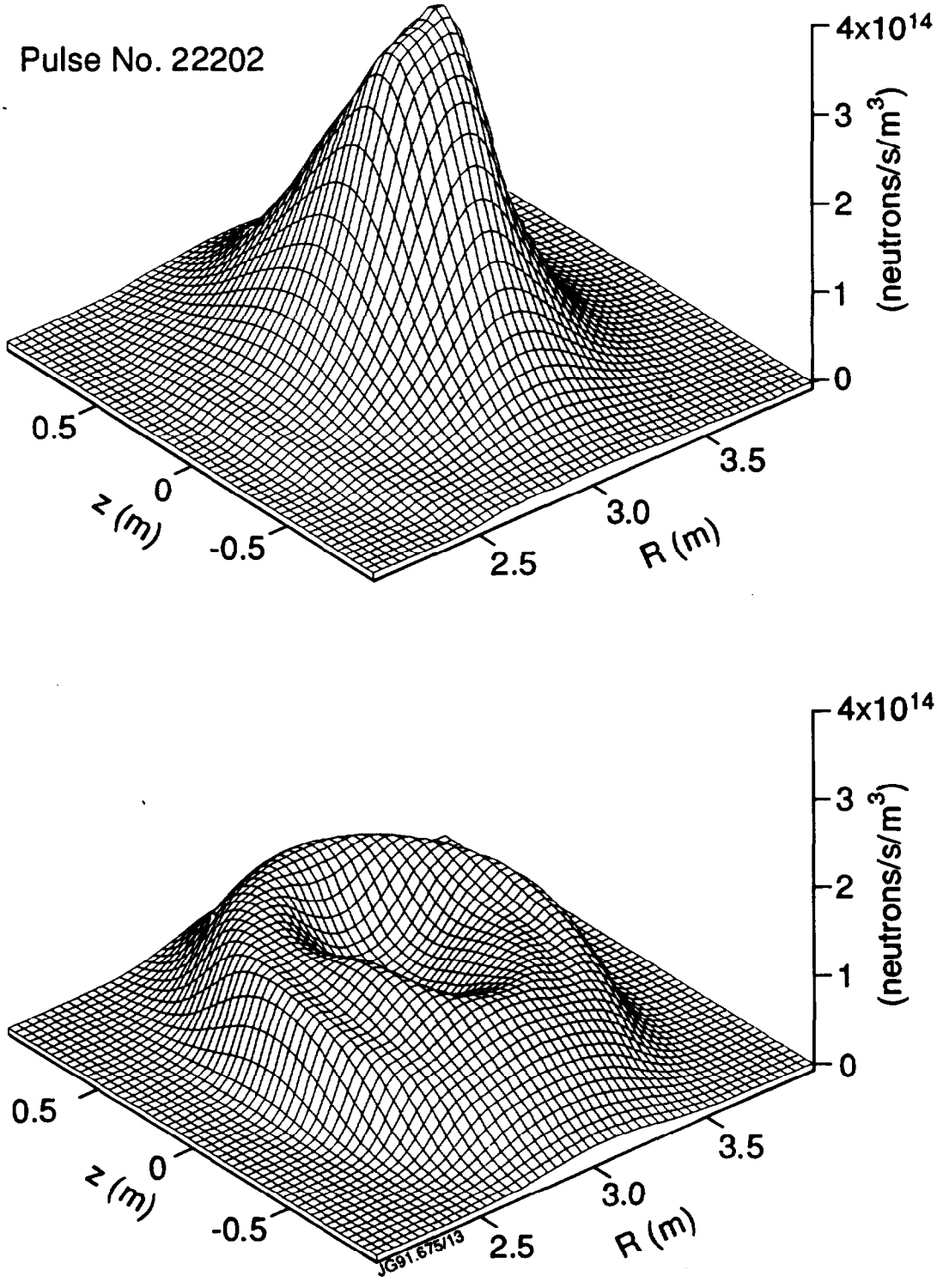


18. Example of Tomographic Reconstruction (Ref. 16) showing the neutron emission profile before and after a sawtooth crash.

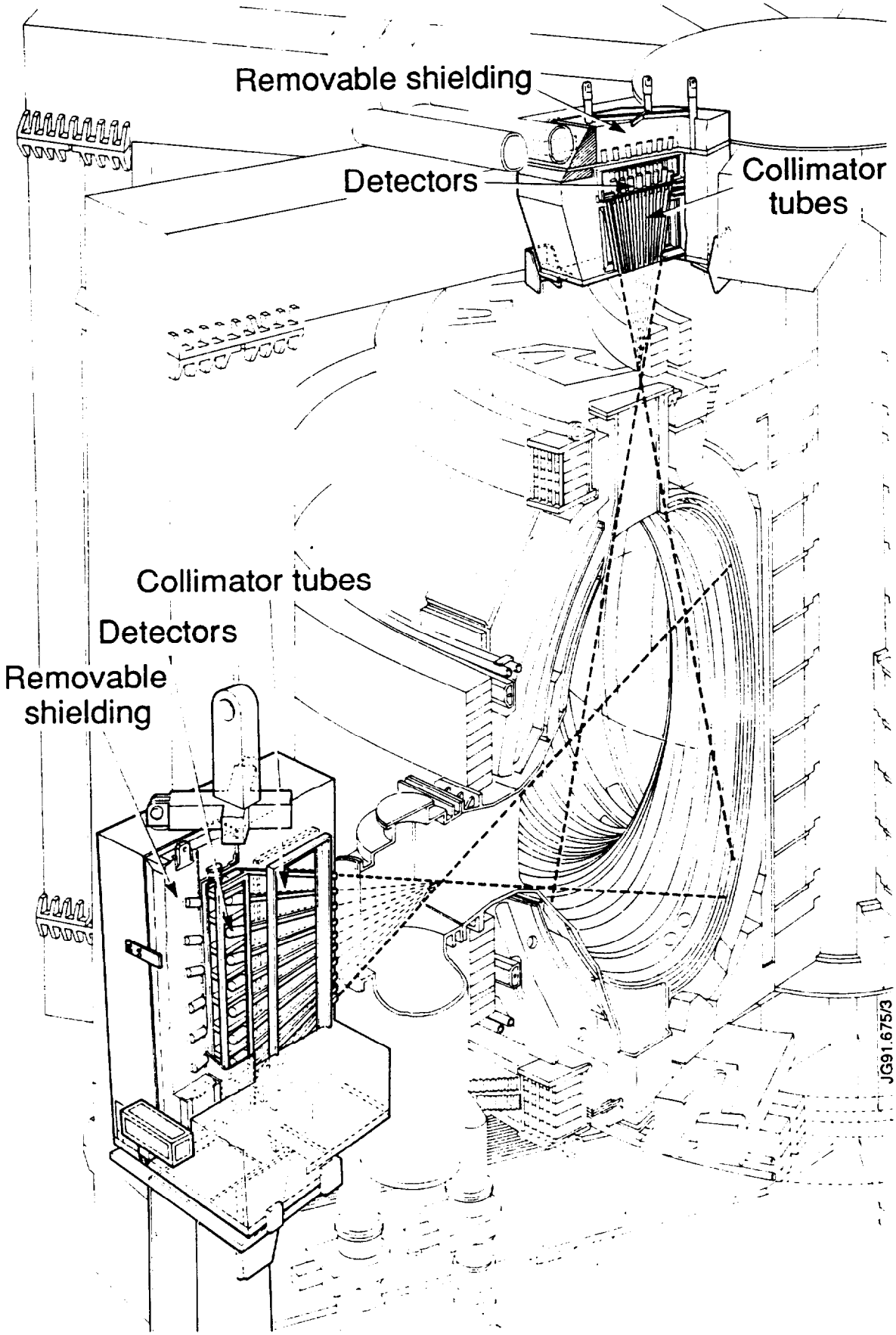


1. Artist's Impression of the JET Neutron Emission Profile Monitor. The location of the 2 bulk shield assemblies are shown relative to the main structure of JET.

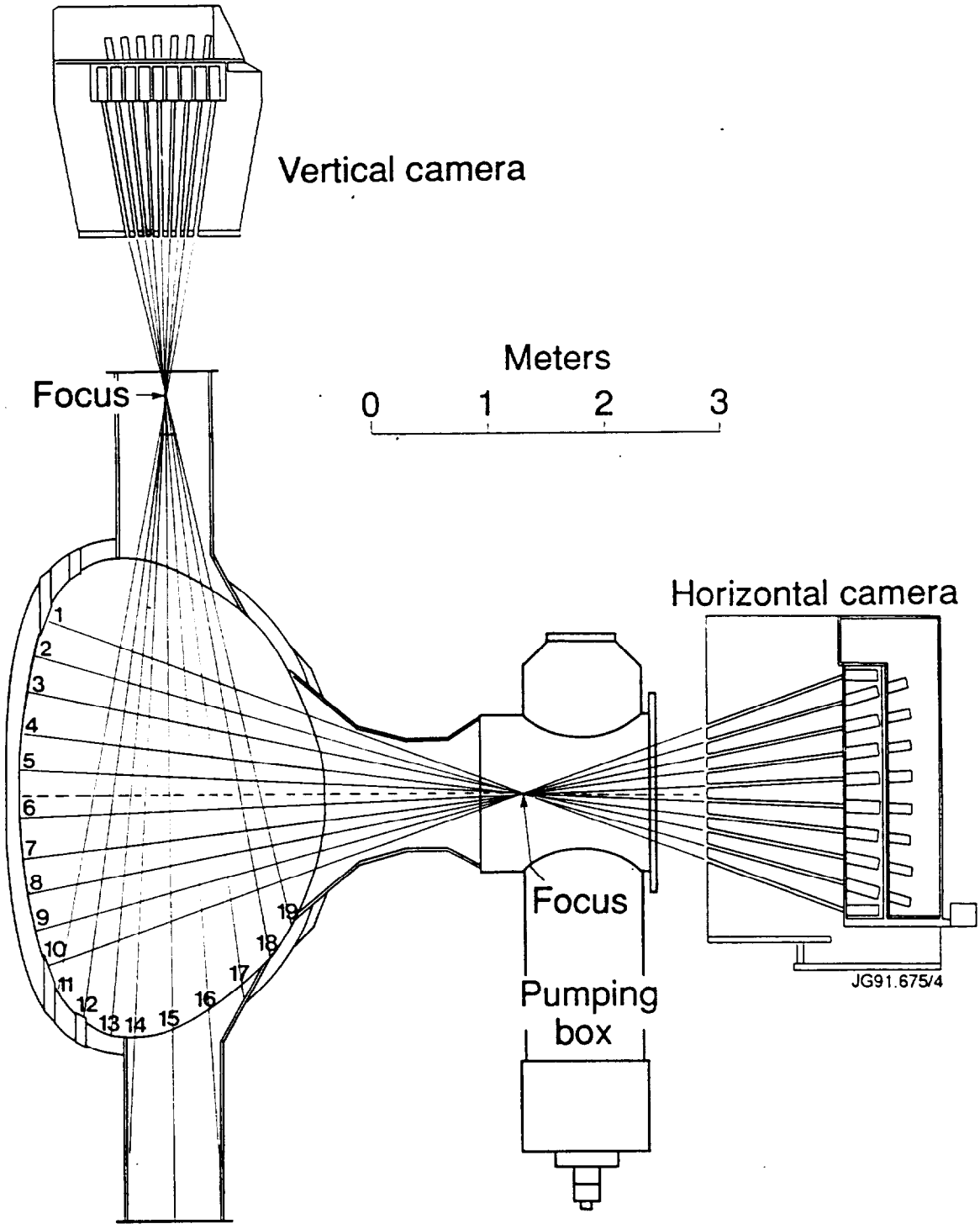


2. Schematic of the JET Neutron Emission Profile Monitor Collimation Geometry. The direct line-of-sight chords illustrate the overall viewing extent within the JET vacuum vessel.

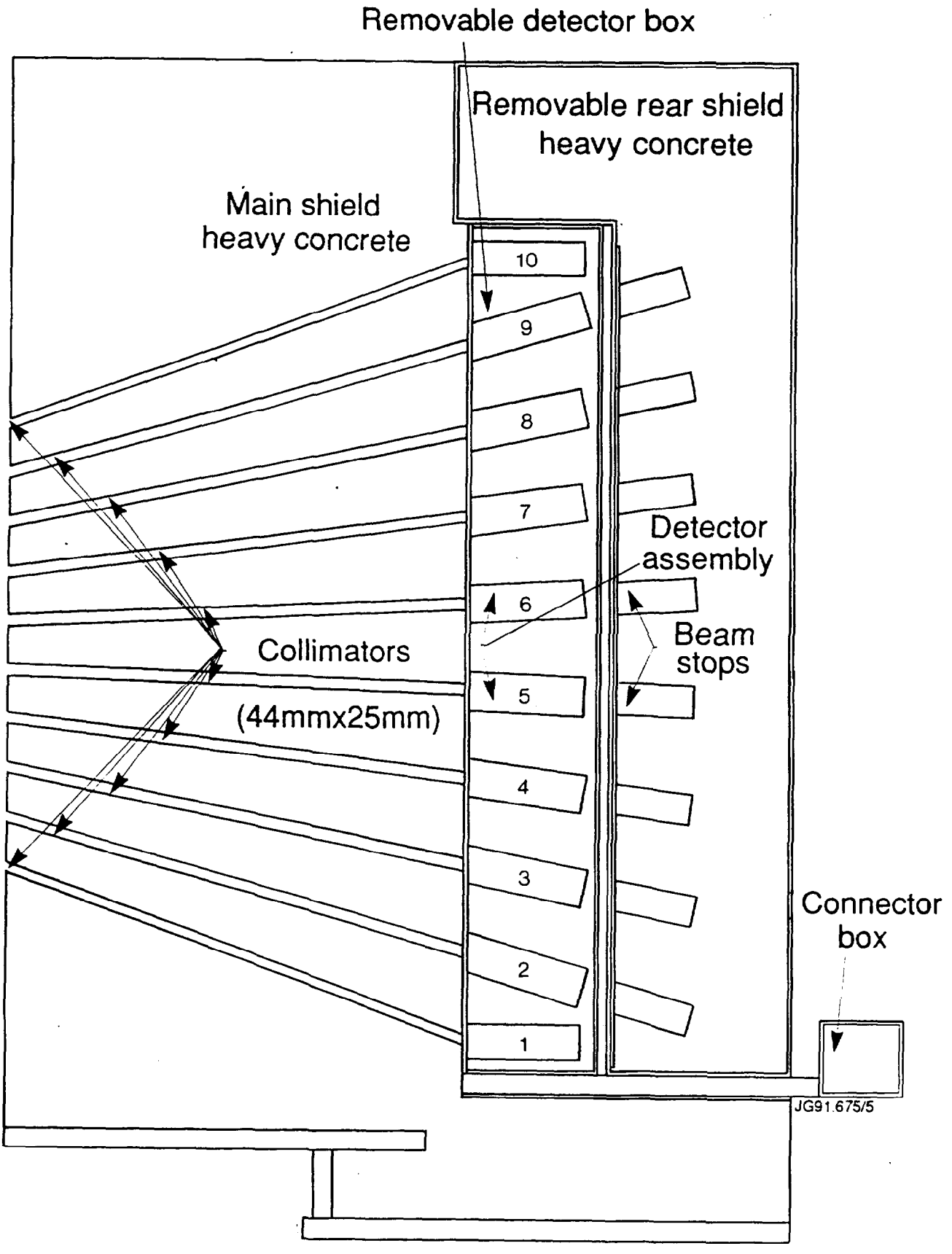


3. Horizontal Camera Shield Assembly ( ≈32 tonnes ). The location of the removable detector box and rear shield are shown relative to the main bulk shield in which are embedded the 10 collimator channels. The removable rear shield contains the neutron beam dumps for 8 of the 10 channels.

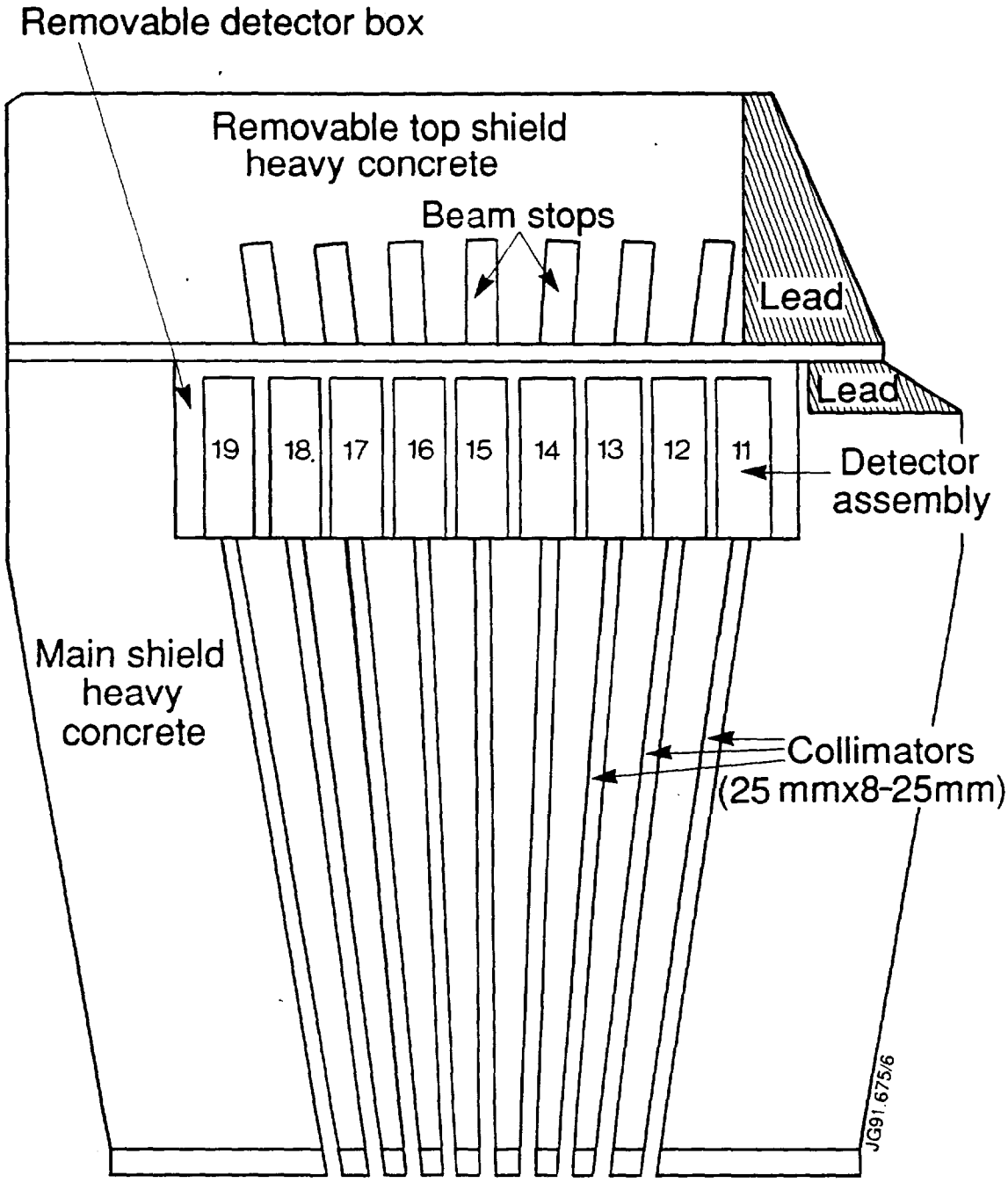


4. Vertical Camera Shield Assembly ( ≈12 tonnes ). The location of the removable detector box and top shield are shown relative to the main bulk shield in which are embedded the 9 collimator channels. The removable top shield contains the neutron beam dumps for 7 of the 9 channels. Additional lead shielding is included to shield against $\gamma$-rays emitted from the adjacent watercooling pipe.

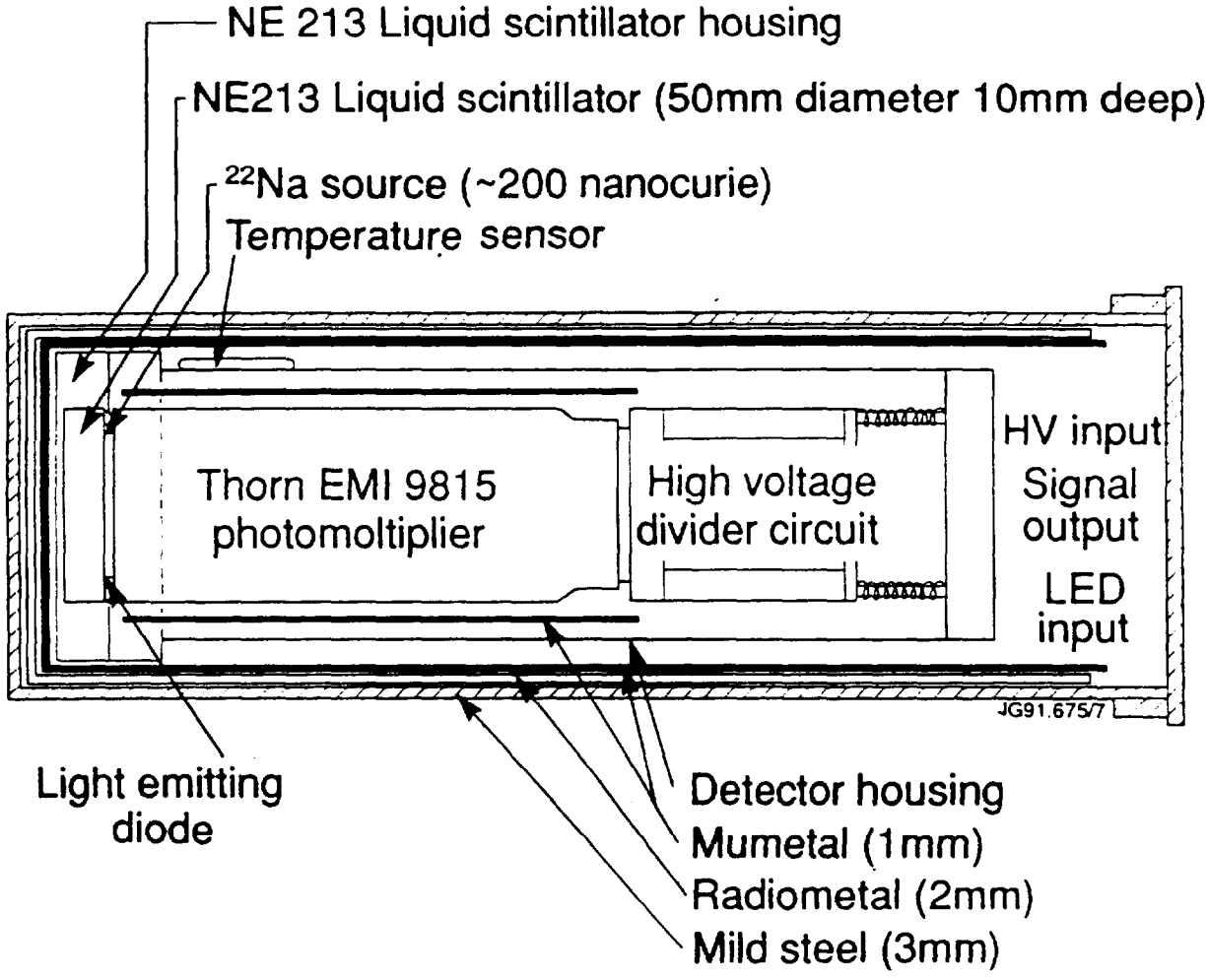


5. Fast Neutron Detector and Triple Magnetic Shield Assembly. This illustrates the magnetic shielding around the neutron detector necessary for operation in the highly fluctuating magnetic fields in the vicinity of JET.

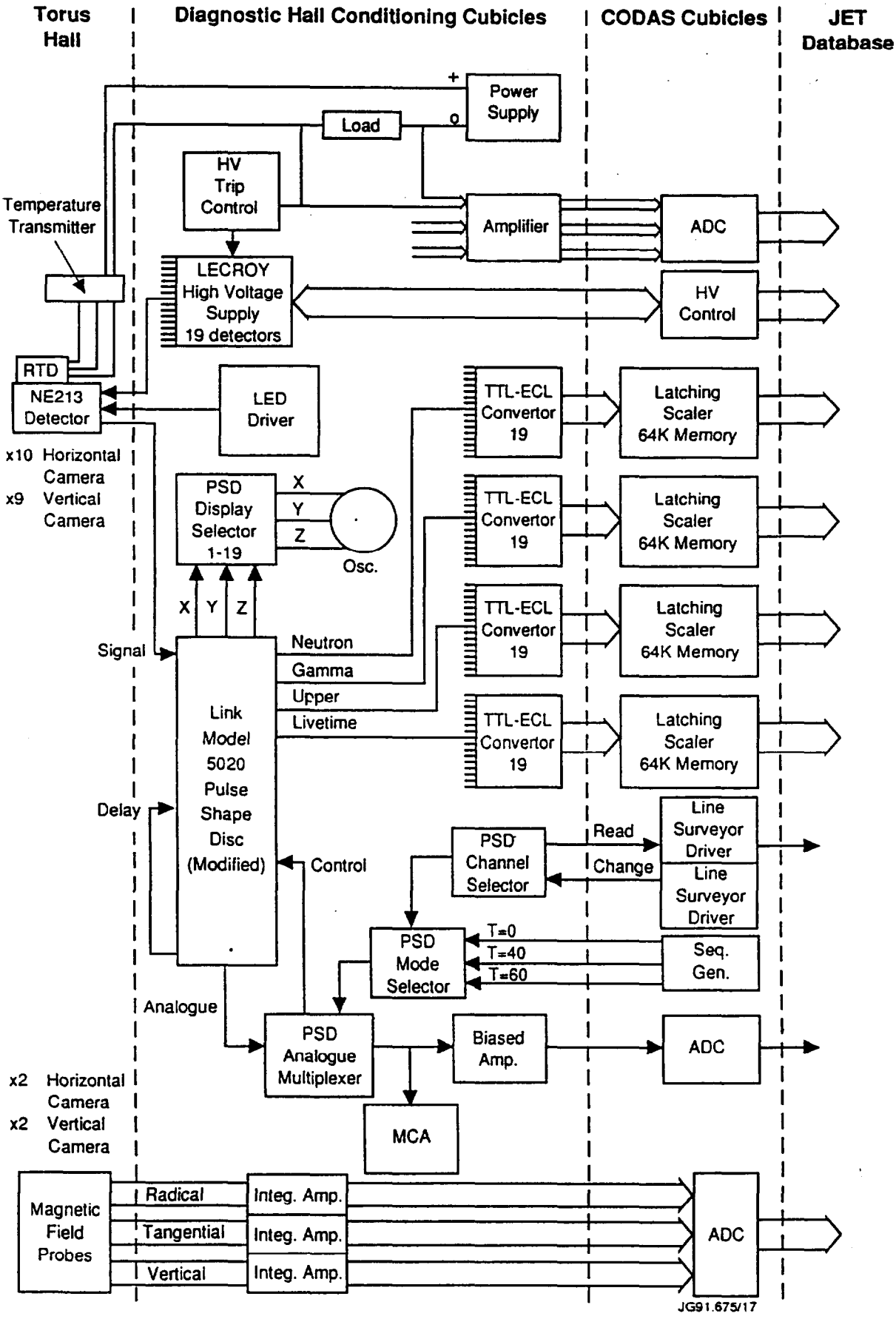


6. *Electronic Schematic of JET Neutron Emission Profile Monitor.* This shows the complete electronic configuration for one neutron detector channel, and its relation to the communal data acquisition modules for storage in the JET database.

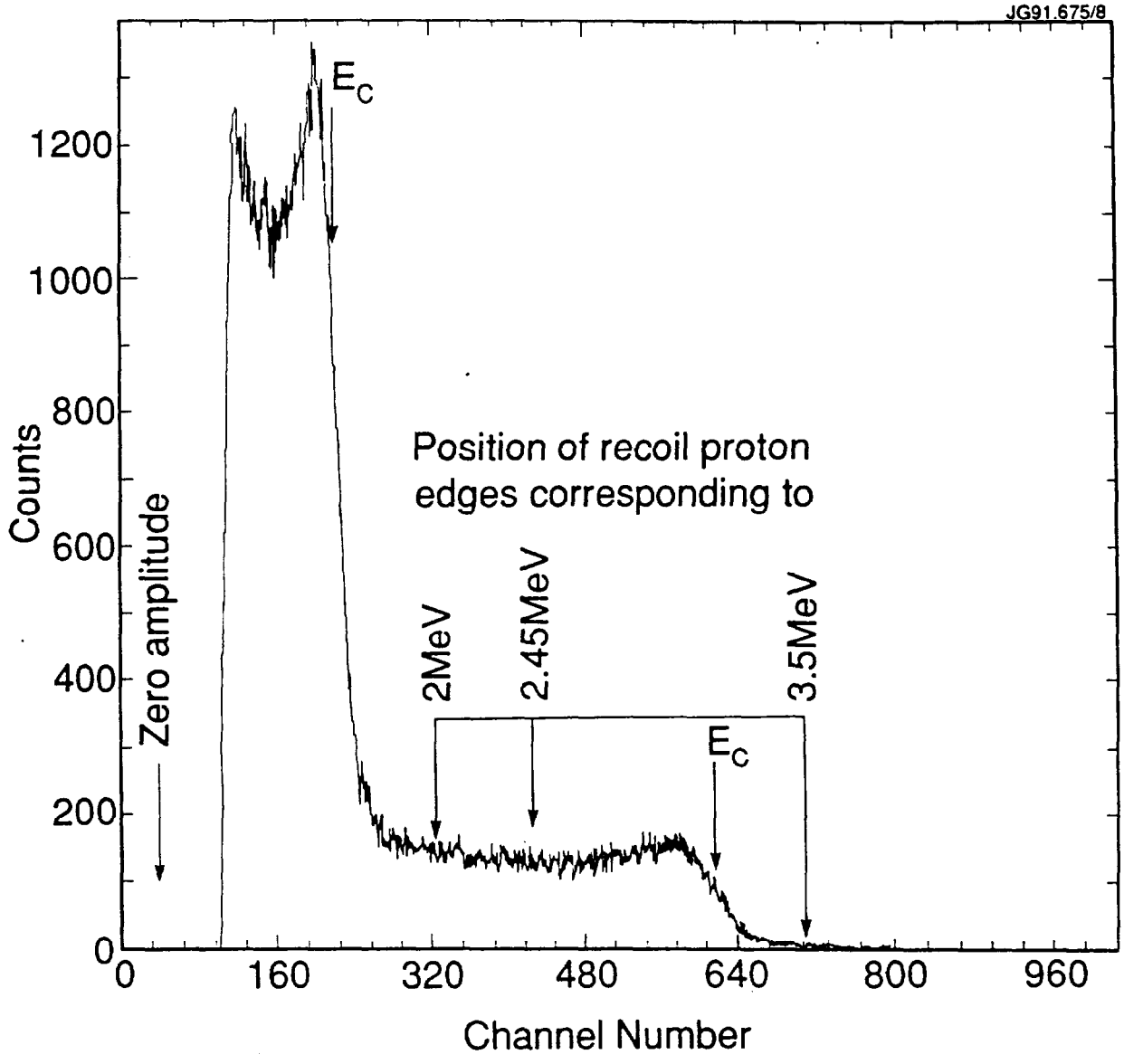


7. $^{22}$Na Pulse Height Spectrum showing Neutron Energy Equivalence. This illustrates the relationship between neutrons and $\gamma$-rays in terms of their equivalent electron energies. The neutron energy bias monitoring technique adopted requires that the UPPER discrimination level be set above the Compton edge of the 1274keV $\gamma$-rays from $^{22}$Na.

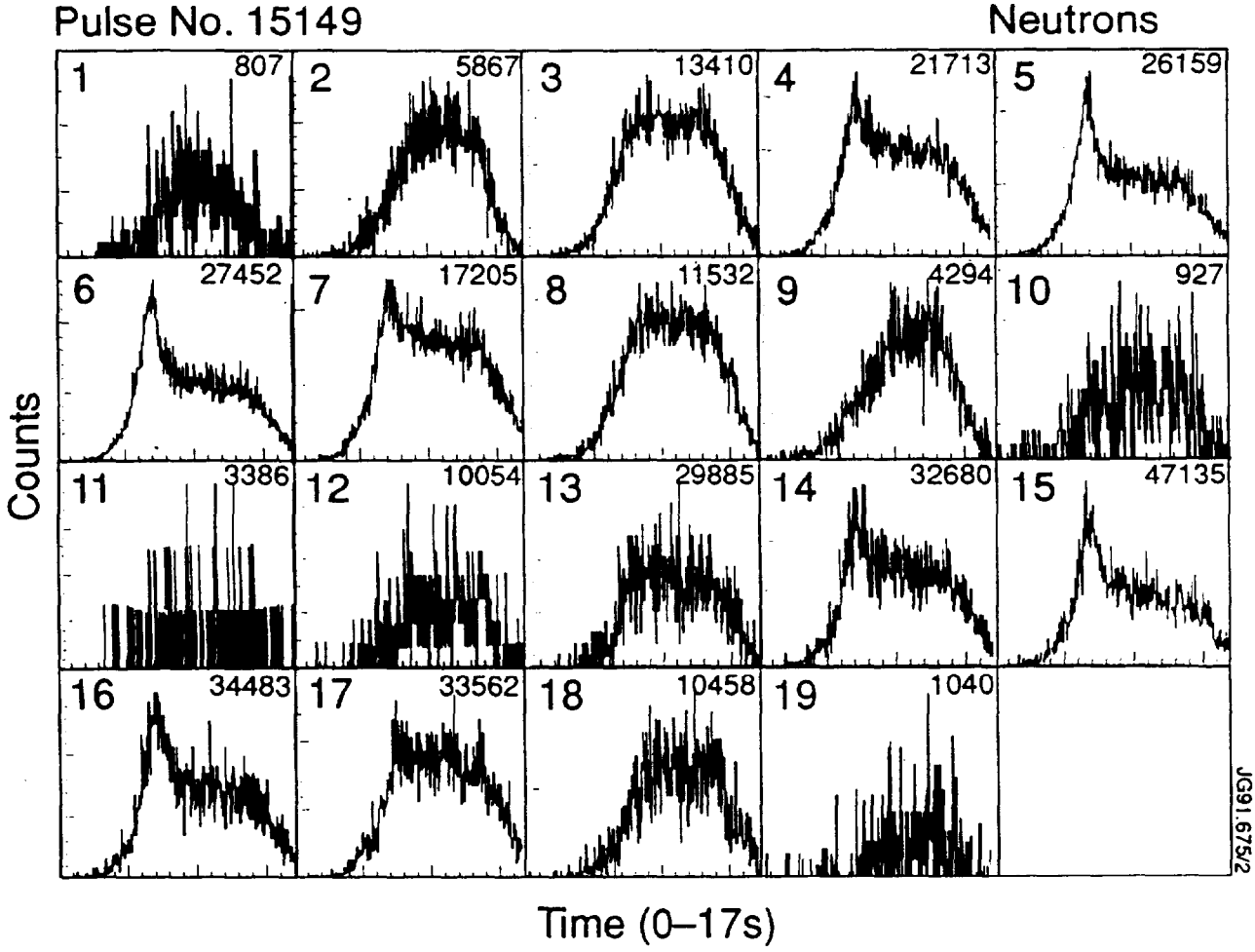


8. Time Dependence of the Neutron Emission in the 19 Individual Channels for a Deuterium Fuelled 5MA Discharge. The traces are corrected for neutron detection efficiency etc. The channel numbers are indicated in the top left hand corners. The total neutron emission observed in the individual channels during the 17s period are indicated in the top right hand corners.

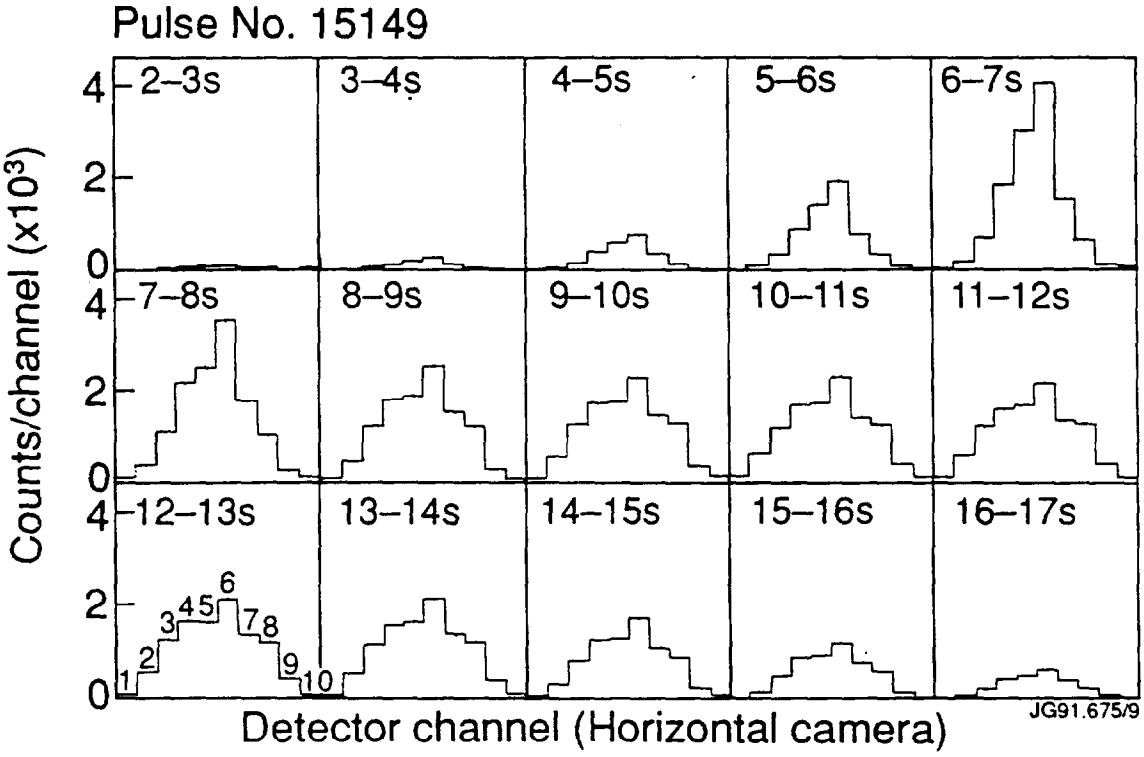


9. Neutron Emission Profiles as seen by the Horizontal Camera in 1s Intervals for the Same Discharge as shown in *Fig. 8*. Time intervals are marked at the top of each profile and the channel number correspondance is indicated in the bottom left hand profile.

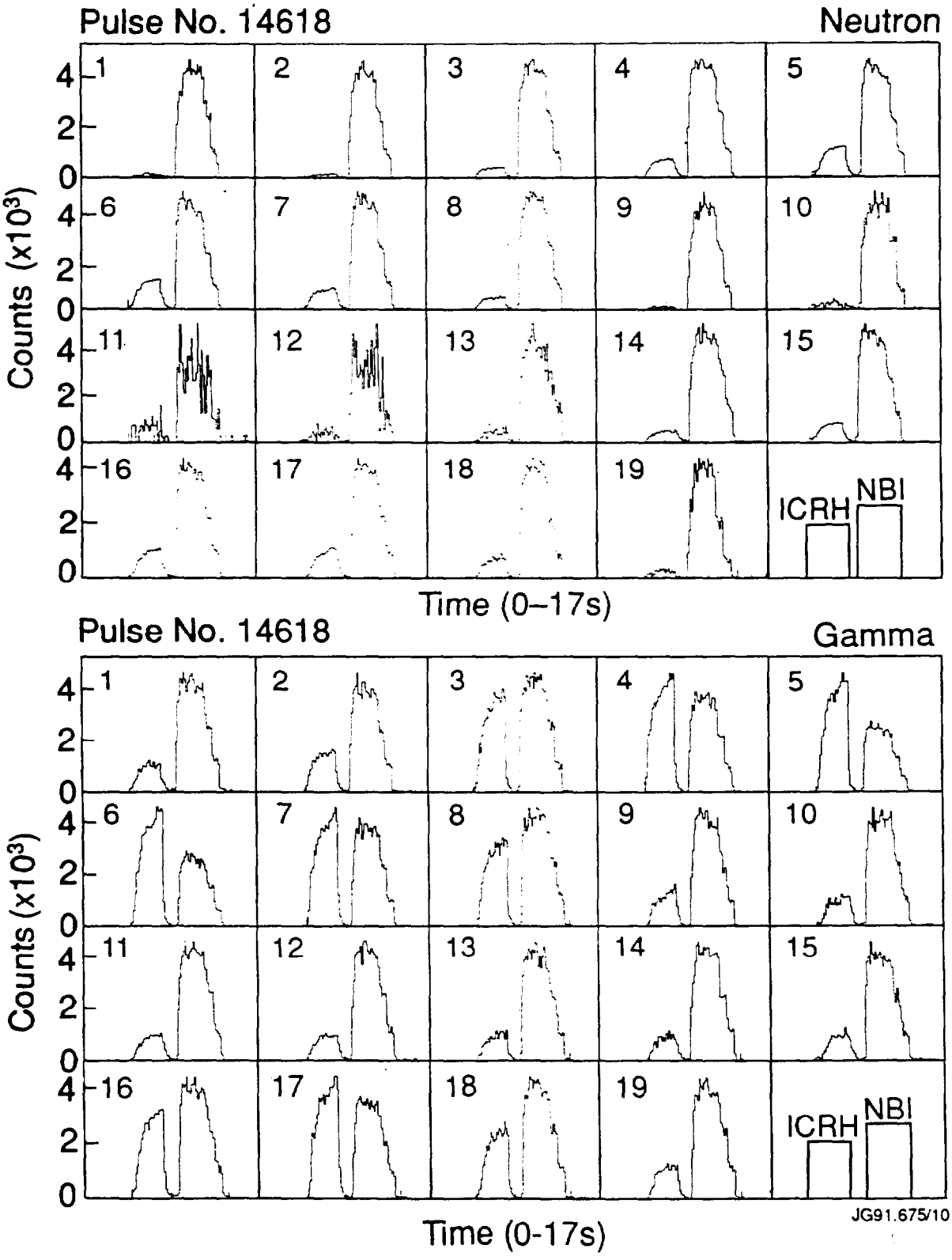


10. Comparison of Neutron and $\gamma$-ray Emission Time Traces during Periods of ICRH (9.5MW $^3$He) and NBI (8MW of 80keV D$^o$). Channel numbers are given in the top left hand corners. The final trace shows the heating waveform. It is clear that the $\gamma$-ray emission in the central channels is strongest during the ICRH period whereas the neutron emission in all channels is strongest during the NBI heating period.

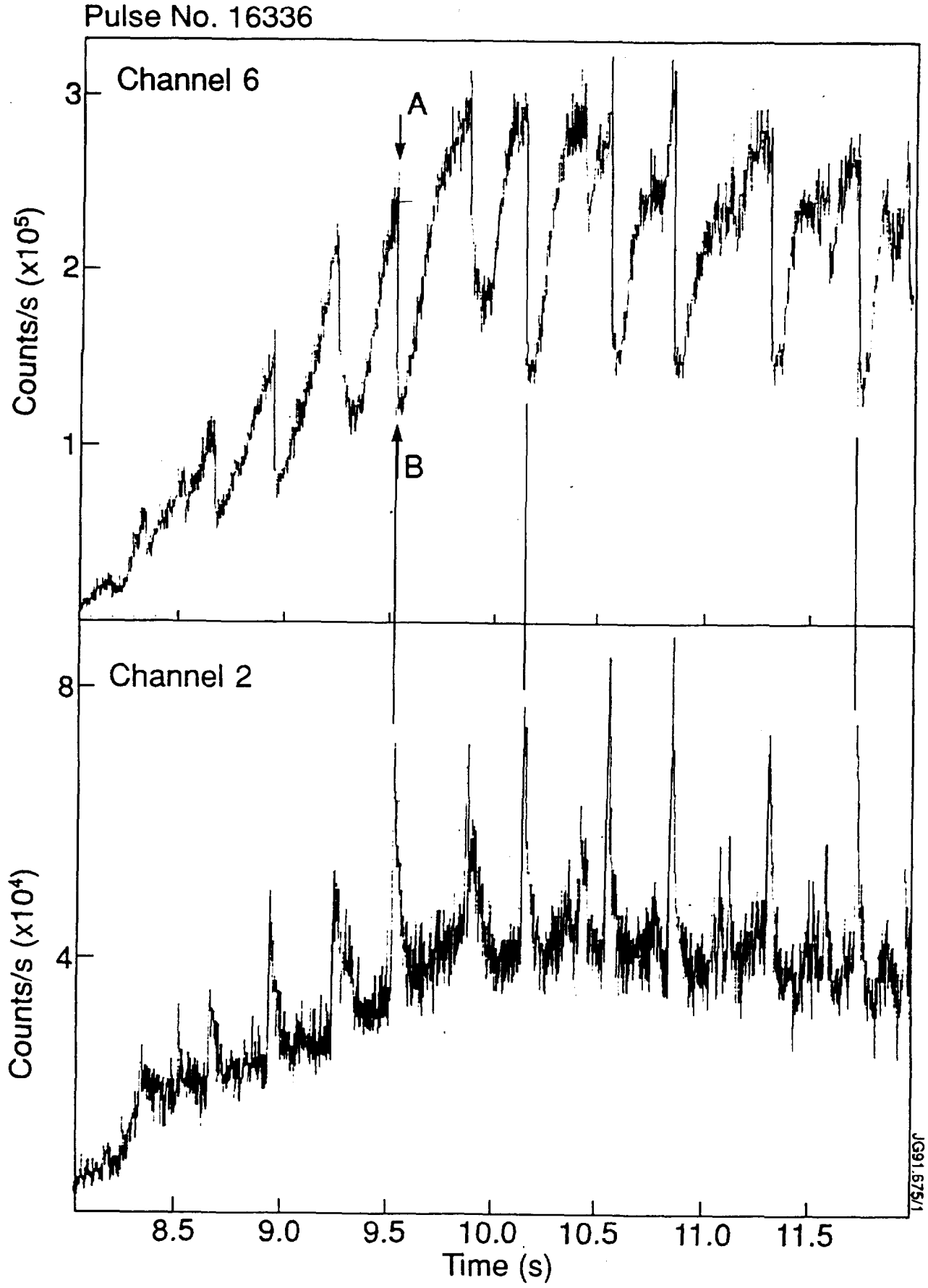


11. Neutron Sawteeth as observed in a Central Channel (Channel 6) and Associated Reversals from an Outer Channel (Channel 2) for a 5MA Deuterium Fuelled Discharge with 9MW of ICRH and 6MW of NBI Heating. The data were acquired in 2.5ms intervals.

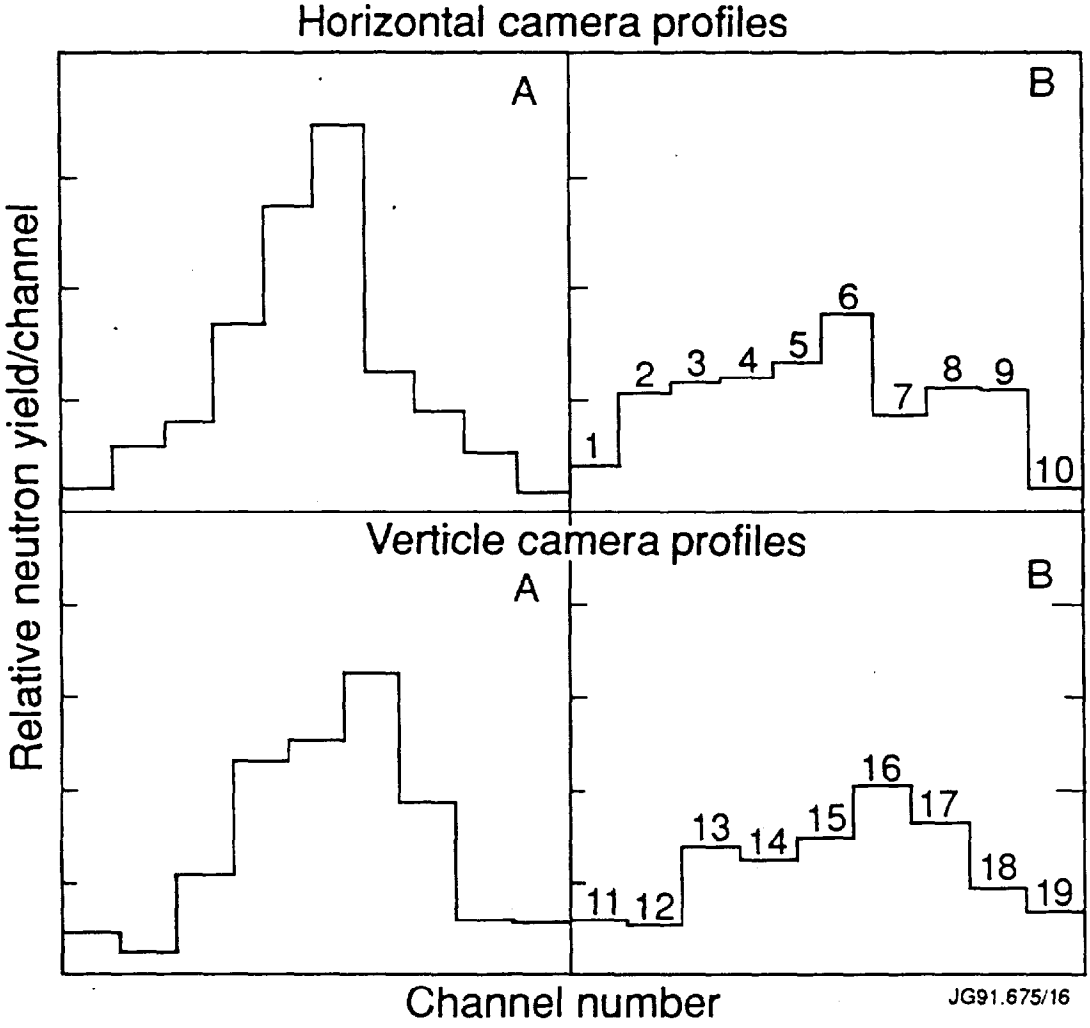


12. Neutron Emission Profiles during a 2.5ms Time Interval Before and After the Sawtooth Marked in *Fig. 11*.

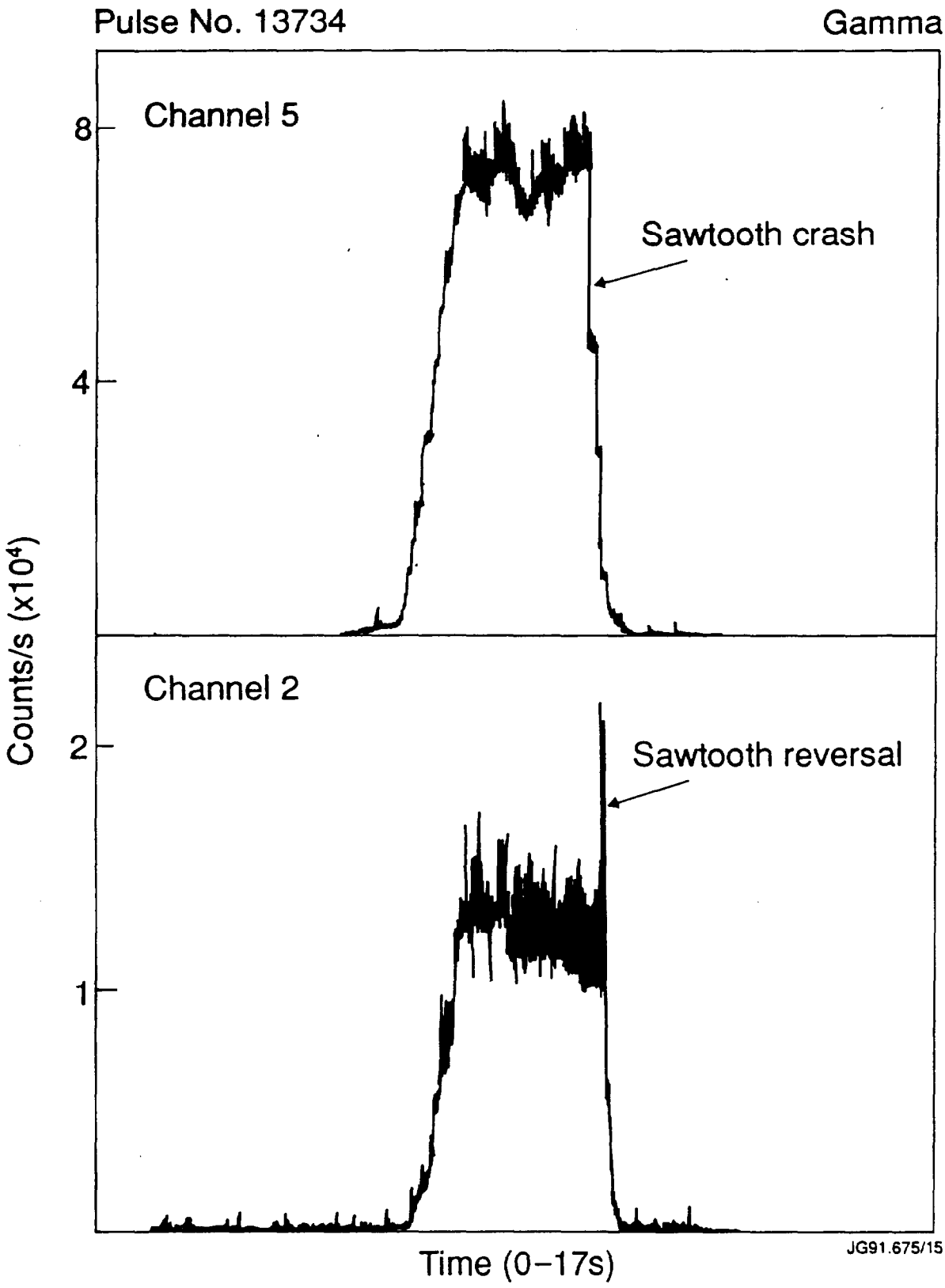


13. A Monster Sawtooth Crash as observed by the $\gamma$-ray Channels 5 and 2. A clear reversal is seen in Channel 2. The observed $\gamma$-rays are due to interactions of energetic RF driven (11MW) $^3$He ions (E > 1MeV) interacting with C impurity ions in the plasma. At the sawtooth crash these fast particles are expelled from the centre of the plasma causing the abrupt increase in $\gamma$-ray detection in the outer channels.

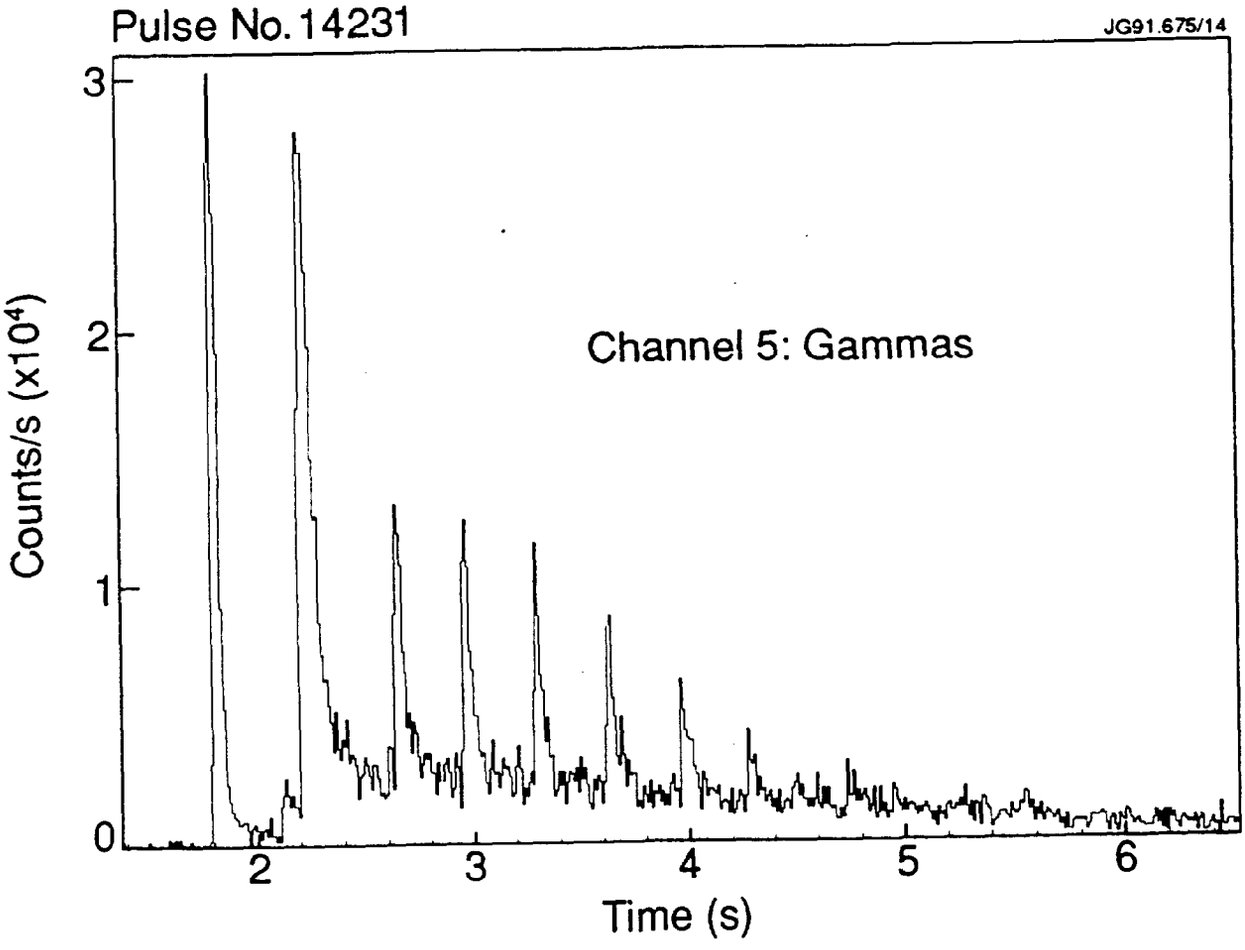


14. Example of a Run-away Electron Dominated Discharge. The periodic interaction of the fast (up to 60 MeV) electrons with the first wall components leads to the generation of bursts of hard X-ray Bremsstrahlung, which is detected in the $\gamma$-ray channels of the cameras.

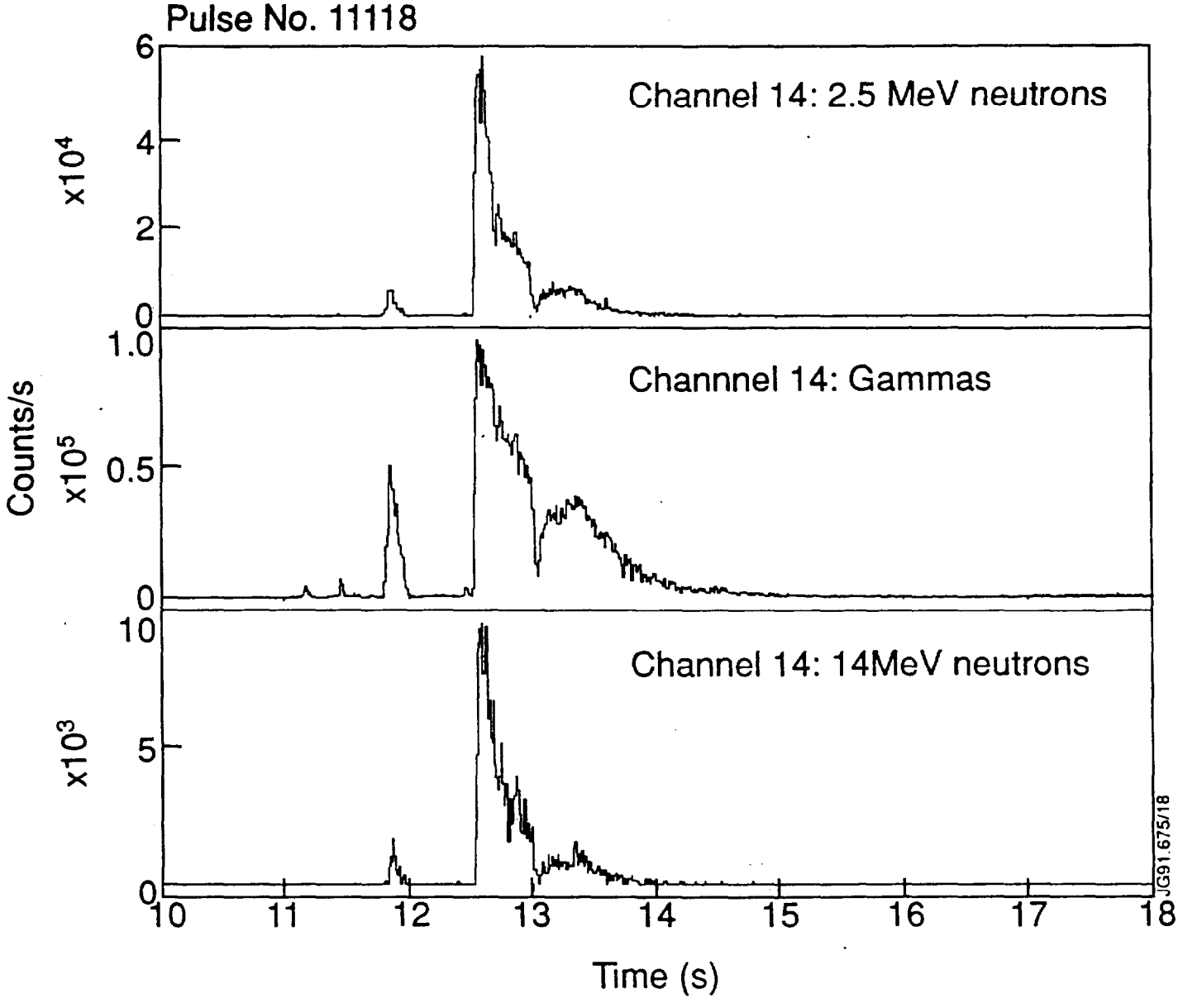


15. Example of Run-away Electrons Observed only in Channel 14. Run-away electrons interact locally with first wall material opposite the line-of-sight of Channel 14 to form bursts of hard X-rays (identified as $\gamma$-rays by the PSD unit) and photoneutrons.

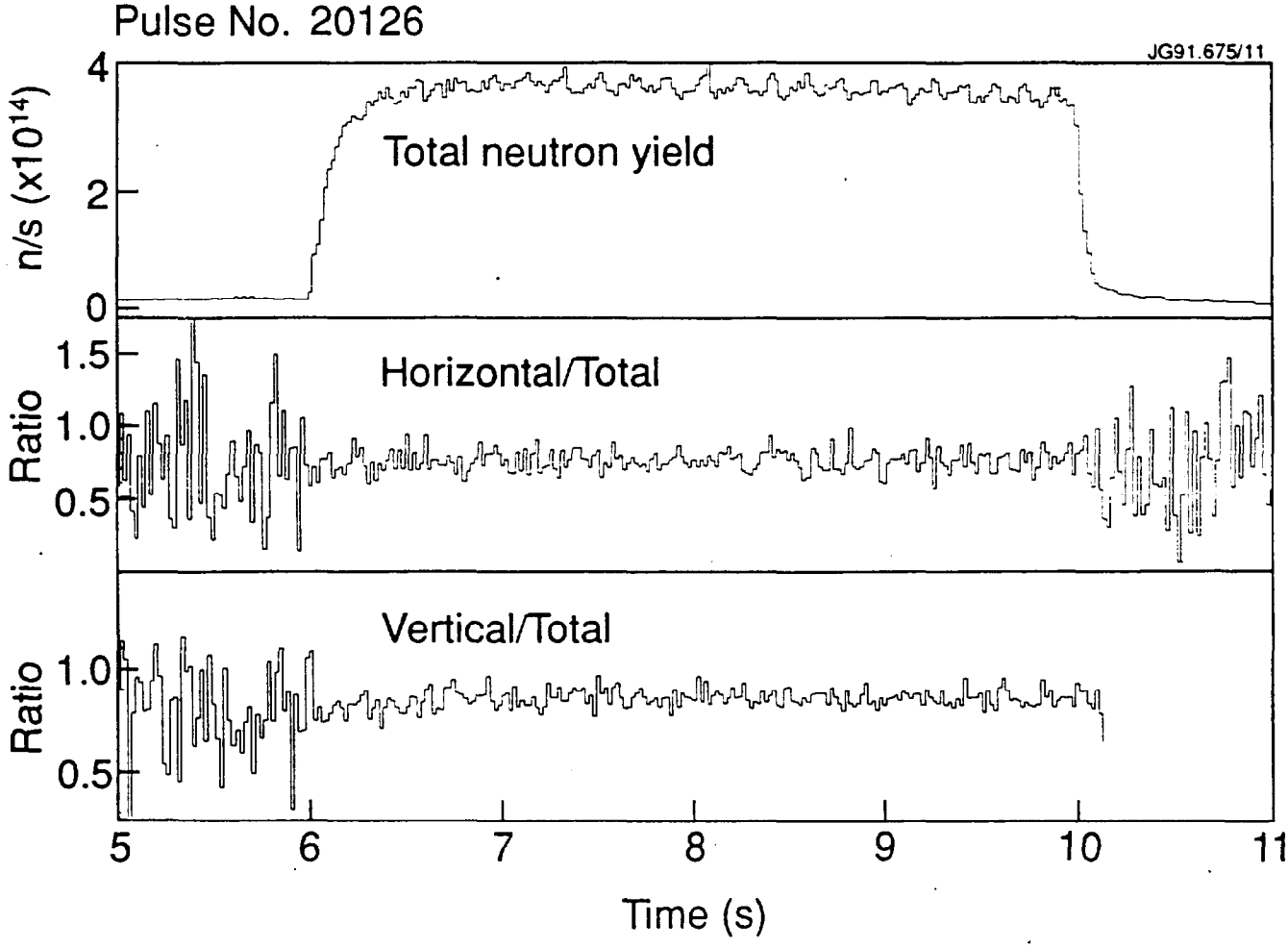


16. Ratios of Measured Neutron Emission for a 2.5MW NBI Discharge. The upper time trace shows the global neutron yield as determined by the time-resolved fission chambers. The middle and lowermost time traces show, respectively, the ratio between the individual camera summations and the global neutron yields. In this case the ratio is constant during the whole of the discharge period associated with significant fusion neutron production.

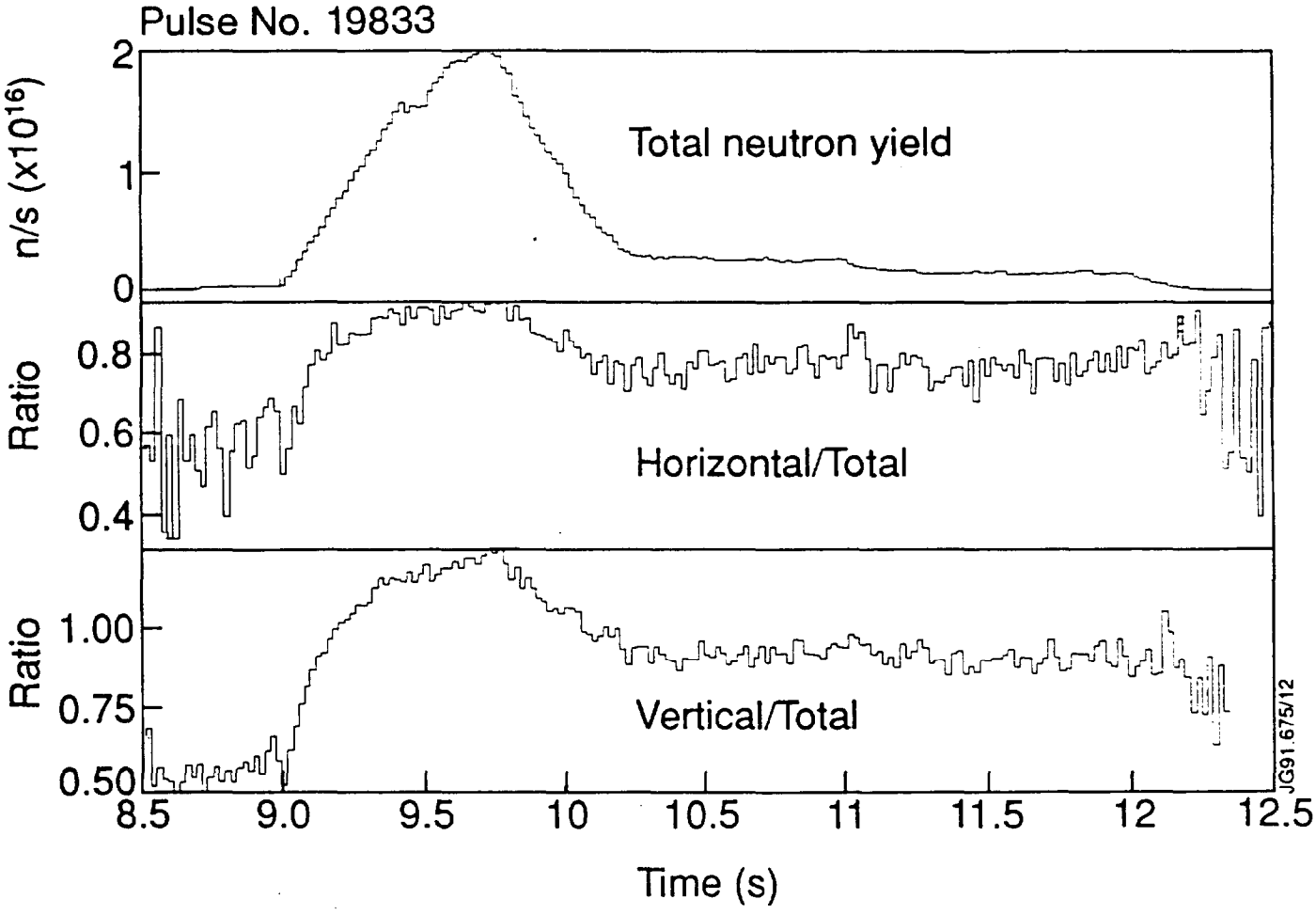


17. Ratios of Measured Neutron Emission for a combined 18MW NBI and 12MW ICRH Discharge. In this case the ratio deviates significantly from a constant during the period of maximum fusion neutron production due to $\gamma$-ray breakthrough effects and the detection of neutrons resulting from nuclear reactions with plasma contaminants. Note the low values during the period before 9s while only ICRH was applied to preheat the plasma.

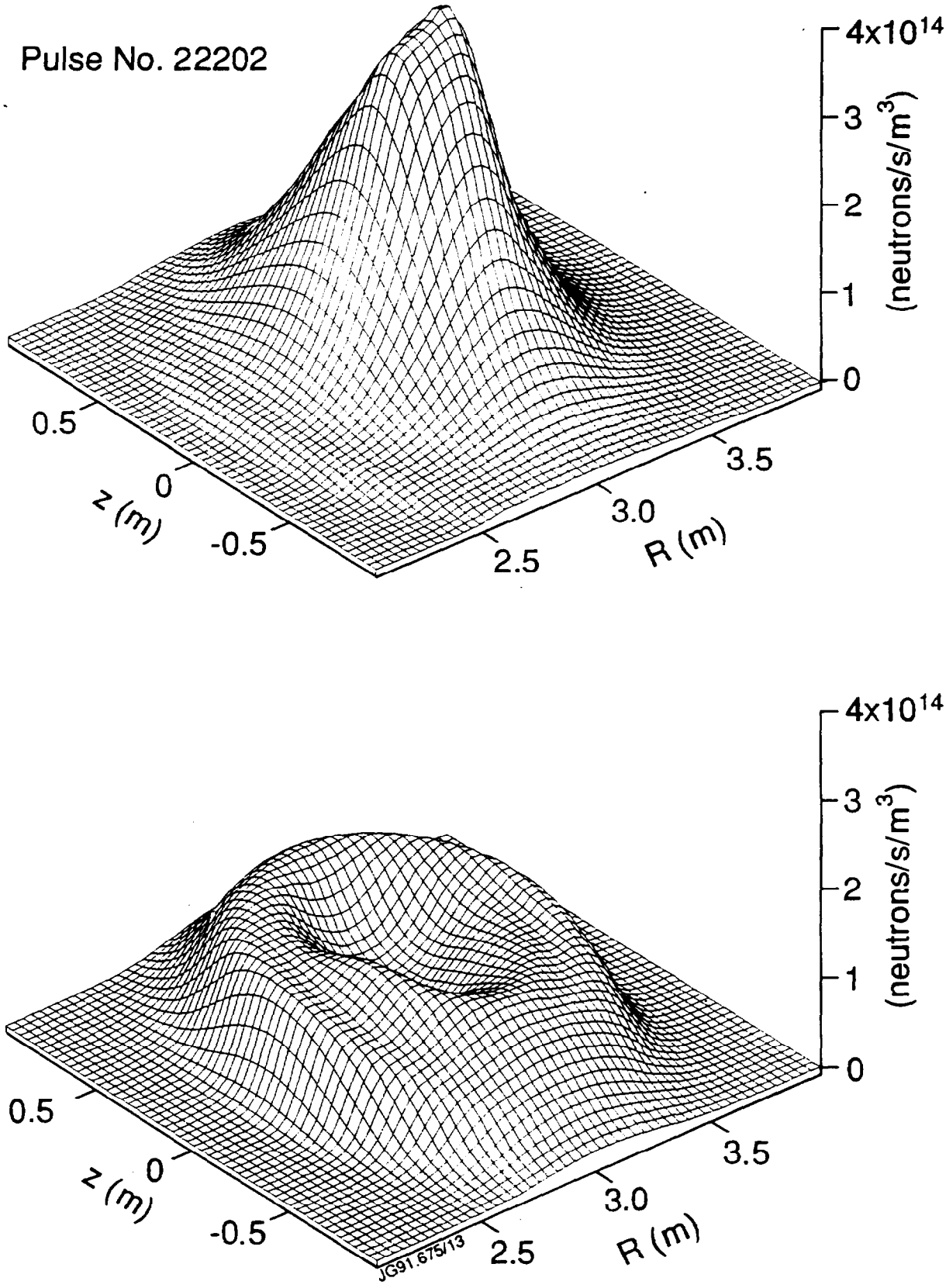


18. Example of Tomographic Reconstruction (Ref. 16) showing the neutron emission profile before and after a sawtooth crash.

## ANNEX

P.-H. REBUT, A. GIBSON, M. HUGUET, J.M. ADAMS[1], B. ALPER, H. ALTMANN, A. ANDERSEN[2], P. ANDREW[3], M. ANGELONE[4], S. ALI-ARSHAD, P. BAIGGER, W. BAILEY, B. BALET, P. BARABASCHI, P. BARKER, R. BARNSLEY[5], M. BARONIAN, D.V. BARTLETT, L. BAYLOR[6], A.C. BELL, G. BENALI, P. BERTOLDI, E. BERTOLINI, V. BHATNAGAR, A.J. BICKLEY, D. BINDER, H. BINDSLEV[2], T. BONICELLI, S.J. BOOTH, G. BOSIA, M. BOTMAN, D. BOUCHER, P. BOUCQUEY, P. BREGER, H. BRELEN, H. BRINKSCHULTE, D. BROOKS, A. BROWN, T. BROWN, M. BRUSATI, S. BRYAN, J. BRZOZOWSKI[7], R. BUCHSE[22], T. BUDD, M. BURES, T. BUSINARO, P. BUTCHER, H. BUTTGEREIT, C. CALDWELL-NICHOLS, D.J. CAMPBELL, P. CARD, G. CELENTANO, C.D. CHALLIS, A.V. CHANKIN[8], A. CHERUBINI, D. CHIRON, J. CHRISTIANSEN, P. CHUILON, R. CLAESEN, S. CLEMENT, E. CLIPSHAM, J.P. COAD, I.H. COFFEY[9], A. COLTON, M. COMISKEY[10], S. CONROY, M. COOKE, D. COOPER, S. COOPER, J.G. CORDEY, W. CORE, G. CORRIGAN, S. CORTI, A.E. COSTLEY, G. COTTRELL, M. COX[11], P. CRIPWELL[12], O. Da COSTA, J. DAVIES, N. DAVIES, H. de BLANK, H. de ESCH, L. de KOCK, E. DEKSNIS, F. DELVART, G.B. DENNE-HINNOV, G. DESCHAMPS, W.J. DICKSON[13], K.J. DIETZ, S.L. DMITRENKO, M. DMITRIEVA[14], J. DOBBING, A. DOGLIO, N. DOLGETTA, S.E. DORLING. P.G. DOYLE, D.F. DÜCHS, H. DUQUENOY, A. EDWARDS, J. EHRENBERG, A. EKEDAHL, T. ELEVANT[7], S.K. ERENTS[11], L.G. ERIKSSON, H. FAJEMIROKUN[12], H. FALTER, J. FREILING[15], F. FREVILLE, C. FROGER, P. FROISSARD, K. FULLARD, M. GADEBERG, A. GALETSAS, T. GALLAGHER, D. GAMBIER, M. GARRIBBA, P. GAZE, R. GIANNELLA, R.D. GILL, A GIRARD, A. GONDHALEKAR, D. GOODALL[11], C. GORMEZANO, N.A. GOTTARDI, C. GOWERS, B.J. GREEN, B. GRIEVSON, R. HAANGE, A. HAIGH, C.J. HANCOCK, P.J. HARBOUR, T. HARTRAMPF, N.C. HAWKES[11], P. HAYNES[11], J.L. HEMMERICH, T. HENDER[11], J. HOEKZEMA, D. HOLLAND, M. HONE, L. HORTON, J. HOW, M. HUART, I. HUGHES, T.P. HUGHES[10], M. HUGON, Y. HUO[16], K. IDA[17], B. INGRAM, M. IRVING, J. JACQUINOT, H. JAECKEL, J.F. JAEGER, G. JANESCHITZ, Z. JANKOVICZ[18], O.N. JARVIS, F. JENSEN, E.M. JONES, H.D. JONES, L.P.D.F. JONES, S. JONES[19], T.T.C. JONES, J.-F. JUNGER, F. JUNIQUE, A. KAYE, B.E. KEEN, M. KEILHACKER, G.J. KELLY, W. KERNER, A. KHUDOLEEV[21], R. KONIG, A. KONSTANTELLOS, M. KOVANEN[20], G. KRAMER[15], P. KUPSCHUS, R. LÄSSER, J.R. LAST, B. LAUNDY, L. LAURO-TARONI, M. LAVEYRY, K. LAWSON[11], M. LENNHOLM, J. LINGERTAT[22], R.N. LITUNOVSKI, A. LOARTE, R. LOBEL, P. LOMAS, M. LOUGHLIN, C. LOWRY, J. LUPO, A.C. MAAS[15], J. MACHUZAK[19], B. MACKLIN, G. MADDISON[11], C.F. MAGGI[23], G. MAGYAR, W. MANDL[22], V. MARCHESE, G. MARCON, F. MARCUS, J. MART, D. MARTIN, E. MARTIN, R. MARTIN-SOLIS[24], P. MASSMANN, G. MATTHEWS, H. McBRYAN, G. McCRACKEN[11], J. McKIVITT, P. MERIGUET, P. MIELE, A. MILLER, J. MILLS, S.F. MILLS, P. MILLWARD, P. MILVERTON, E. MINARDI[4], R. MOHANTI[25], P.L. MONDINO, D. MONTGOMERY[26], A. MONTVAI[27], P. MORGAN, H. MORSI, D. MUIR, G. MURPHY, R. MYRNÄS[28], F. NAVE[29], G. NEWBERT, M. NEWMAN, P. NIELSEN, P. NOLL, W. OBERT, D. O'BRIEN, J. ORCHARD, J. O'ROURKE, R. OSTROM, M. OTTAVIANI, M. PAIN, F. PAOLETTI, S. PAPASTERGIOU, W. PARSONS, D. PASINI, D. PATEL, A. PEACOCK, N. PEACOCK[11], R.J.M. PEARCE, D. PEARSON[12], J.F. PENG[16], R. PEPE DE SILVA, G. PERINIC, C. PERRY, M. PETROV[21], M.A. PICK, J. PLANCOULAINE, J.-P POFFÉ, R. PÖHLCHEN, F. PORCELLI, L. PORTE[13], R. PRENTICE, S. PUPPIN, S. PUTVINSKII[8], G. RADFORD[30], T. RAIMONDI, M.C. RAMOS DE ANDRADE, R. REICHLE, J. REID, S. RICHARDS, E. RIGHI, F. RIMINI, D. ROBINSON[11], A. ROLFE, R.T. ROSS, L. ROSSI, R. RUSS, P. RUTTER, H.C. SACK, G. SADLER, G. SAIBENE, J.L. SALANAVE, G. SANAZZARO, A. SANTAGIUSTINA, R. SARTORI, C. SBORCHIA, P. SCHILD, M. SCHMID, G. SCHMIDT[31], B. SCHUNKE, S.M. SCOTT, L. SERIO, A SIBLEY, R. SIMONINI, A.C.C. SIPS, P. SMEULDERS, R. SMITH, R. STAGG, M. STAMP, P. STANGEBY[3], R. STANKIEWICZ[32], D.F. START, C.A. STEED, D. STORK, P.E. STOTT, P. STUBBERFIELD, D. SUMMERS, H. SUMMERS[13], L. SVENSSON, J.A. TAGLE[33], M. TALBOT, A. TANGA, A. TARONI, C. TERELLA, A TERRINGTON, A TESINI, P.R. THOMAS, E. THOMPSON, K. THOMSEN, F. TIBONE, A. TISCORNIA, P. TREVALION, B. TUBBING, P. VAN BELLE, H. VAN DER BEKEN, G. VLASES, M. VON HELLERMANN, T. WADE, C. WALKER, R. WALTON[31], D. WARD, M.L. WATKINS, N. WATKINS, M.J. WATSON, S. WEBER[34], J. WESSON, T.J. WIJNANDS, J. WILKS, D. WILSON, T. WINKEL, R. WOLF, D. WONG, C. WOODWARD, Y. WU[35], M. WYKES, D. YOUNG, I.D. YOUNG, L. ZANNELLI, A. ZOLFAGHARI[19], W. ZWINGMANN

[1] Harwell Laboratory, UKAEA, Harwell, Didcot, Oxfordshire, UK.
[2] Risø National Laboratory, Roskilde, Denmark.
[3] Institute for Aerospace Studies, University of Toronto, Downsview, Ontario, Canada.
[4] ENEA Frascati Energy Research Centre, Frascati, Rome, Italy.
[5] University of Leicester, Leicester, UK.
[6] Oak Ridge National Laboratory, Oak Ridge, TN, USA.
[7] Royal Institute of Technology, Stockholm, Sweden.
[8] I.V. Kurchatov Institute of Atomic Energy, Moscow, Russian Federation.
[9] Queens University, Belfast, UK.
[10] University of Essex, Colchester, UK.
[11] Culham Laboratory, UKAEA, Abingdon, Oxfordshire, UK.
[12] Imperial College of Science, Technology and Medicine, University of London, London, UK.
[13] University of Strathclyde, Glasgow, UK.
[14] Keldysh Institute of Applied Mathematics, Moscow, Russian Federation.
[15] FOM-Institute for Plasma Physics "Rijnhuizen", Nieuwegein, Netherlands.
[16] Institute of Plasma Physics, Academia Sinica, Hefei, Anhui Province, China.
[17] National Institute for Fusion Science, Nagoya, Japan.
[18] Soltan Institute for Nuclear Studies, Otwock/Świerk, Poland.
[19] Plasma Fusion Center, Massachusetts Institute of Technology, Boston, MA, USA.
[20] Nuclear Engineering Laboratory, Lappeenranta University, Finland.
[21] A.F. Ioffe Physico-Technical Institute, St. Petersburg, Russian Federation.
[22] Max-Planck-Institut für Plasmaphysik, Garching, Germany.
[23] Department of Physics, University of Milan, Milan, Italy.
[24] Universidad Complutense de Madrid, Madrid, Spain.
[25] North Carolina State University, Raleigh, NC, USA.
[26] Dartmouth College, Hanover, NH, USA.
[27] Central Research Institute for Physics, Budapest, Hungary.
[28] University of Lund, Lund, Sweden.
[29] Laboratorio Nacional de Engenharia e Tecnologia Industrial, Sacavem, Portugal.
[30] Institute of Mathematics, University of Oxford, Oxford, UK.
[31] Princeton Plasma Physics Laboratory, Princeton University, Princeton, NJ, USA.
[32] RCC Cyfronet, Otwock/Świerk, Poland,
[33] Centro de Investigaciones Energéticas, Medioambientales y Tecnológicas, Madrid, Spain.
[34] Freie Universität, Berlin, Germany.
[35] Insitute for Mechanics, Academia Sinica, Beijing, China.